Robust, persistent adaptive immune responses to SARS-CoV-2 in the oropharyngeal lymphoid tissue of children

Kalpana Manthiram (✉ kalpana.manthiram@nih.gov)

   NIAID/National Institutes of Health

Qin Xu

   NIAID/National Institutes of Health   https://orcid.org/0000-0003-1812-3108

Pedro Milanez-Almeida

   National Institute of Allergy and Infectious Diseases   https://orcid.org/0000-0001-8285-957X

Andrew Martins

   NIH   https://orcid.org/0000-0002-1832-1924

Andrea Radtke

   NIAID, NIH   https://orcid.org/0000-0003-4379-8967

Kenneth Hoehn

   Department of Pathology, Yale University School of Medicine   https://orcid.org/0000-0003-0411-4307

Jinguo Chen

   National Institute of Allergy and Infectious Diseases

Can Liu

   National Institutes of Health   https://orcid.org/0000-0002-8411-3891

Juanjie Tang

   CBER/Food and Drug Administration

Gabrielle Grubbs

   FDA   https://orcid.org/0000-0003-4302-9535

Sydney Stein

   CC/National Institutes of Health   https://orcid.org/0000-0002-0259-4485

Sabrina Ramelli

   CC/National Institutes of Health

Juraj Kabat

   National Institutes of Health

Hengameh Behzadpour

   Children's National Hospital

Maria Karkanitsa

   NIBIB/National Institutes of Health

Jacquelyn Spathies

NIBIB/National Institutes of Health

Heather Kalish
NIBIB/National Institutes of Health

Lela Kardava
National Institute of Allergy & Infectious Disease   https://orcid.org/0000-0001-9135-6026

Martha Kirby
NHGRI/National Institutes of Health

Foo Cheung
Trans-NIH Center for Human Immunology, Autoimmunity, and Inflammation (CHI)

Silvia Preite
National Institutes of Health

Patrick Duncker
Cytek

Nahir Romero
Children's National Hospital

Diego Preciado
Children's National Hospital

Lyuba Gitman
Children's National Hospital

Galina Koroleva
NIAID/National Institutes of Health

Grace Smith
NCI/National Institutes of Health   https://orcid.org/0000-0001-6381-0391

Arthur Shaffer
NCI/National Institutes of Health

Ian McBain
NIAID/National Institutes of Health

Stefania Pittaluga
NIH   https://orcid.org/0000-0001-7688-1439

Ronald Germain
National Institute of Allergy and Infectious Diseases, National Institutes of Health
https://orcid.org/0000-0003-1495-9143

Richard Apps
University of Cambridge

Kaitlyn Sadtler
NIBIB/National Institutes of Health

Susan Moir
NIAID/National Institutes of Health

Daniel Chertow

National Institutes of Health   https://orcid.org/0000-0002-1675-1728

Steven Kleinstein

Yale University   https://orcid.org/0000-0003-4957-1544

Surender Khurana

Food and Drug Administration   https://orcid.org/0000-0002-0593-7965

John Tsang

National Institutes of Health   https://orcid.org/0000-0003-3186-3047

Pamela Mudd

Children's National Hospital

Pamela Schwartzberg

National Institute of Allergy and Infectious Diseases   https://orcid.org/0000-0001-6318-9187

Article

Keywords:

Robust, persistent adaptive immune responses to SARS-CoV-2 in oropharyngeal

lymphoid tissue of children

Qin Xu[1], Pedro Milanez-Almeida[2#], Andrew J. Martins[3#], Andrea J. Radtke[4#], Kenneth B. Hoehn[5#], Jinguo Chen[2], Can Liu[3], Juanjie Tang[6], Gabrielle Grubbs[6], Sydney Stein[7,8], Sabrina Ramelli[7], Juraj Kabat[4], Hengameh Behzadpour[9], Maria Karkanitsa[10], Jacquelyn Spathies[11], Heather Kalish[11], Lela Kardava[12], Martha Kirby[13], Foo Cheung[2], Silvia Preite[1], Patrick C. Duncker[14], Nahir Romero[15], Diego Preciado[9,15], Lyuba Gitman[9,15], Galina Koroleva[2], Grace Smith[16], Arthur Shaffer[17], Ian T. McBain[1], Stefania Pittaluga[16], Ronald N. Germain[4,18], Richard Apps[2], Kaitlyn Sadtler[10], Susan Moir[12], Daniel S. Chertow[7,8], Steven H. Kleinstein[5,19,20], Surender Khurana[6], John S. Tsang[2,3], Pamela Mudd[9,15], Pamela L. Schwartzberg[1,13]*, Kalpana Manthiram[1]*

[1] Cell Signaling and Immunity Section, Laboratory of Immune System Biology (LISB), National Institute of Allergy and Infectious Diseases (NIAID), National Institutes of Health (NIH), Bethesda, MD
[2] Center for Human Immunology, NIAID, NIH, Bethesda, MD
[3] Multiscale Systems Biology Section, LISB, NIAID, NIH, Bethesda, MD
[4] Center for Advanced Tissue Imaging, LISB, NIAID, NIH Bethesda, MD
[5] Department of Pathology, Yale School of Medicine, New Haven, CT
[6] Division of Viral Products, Center for Biologics Evaluation and Research (CBER), Food and Drug Administration (FDA), Silver Spring, MD
[7] Emerging Pathogens Section, Critical Care Medicine Department, Clinical Center (CC), NIH, Bethesda, MD
[8] Laboratory of Immunoregulation, NIAID, NIH, Bethesda, MD
[9] Division of Pediatric Otolaryngology, Children's National Hospital, Washington, DC
[10] Laboratory of Immuno-Engineering, National Institute of Biomedical Imaging and Bioengineering (NIBIB), NIH, Bethesda, MD
[11] Trans-NIH Shared Resource on Biomedical Engineering and Physical Science, NIBIB, NIH, Bethesda, MD
[12] B-cell Immunology Section, Laboratory of Immunoregulation, NIAID, NIH, Bethesda, MD
[13] National Human Genome Research Institute (NHGRI), NIH, Bethesda, MD
[14] Cytek Biosciences, Fremont, CA
[15] Division of Otolaryngology, Department of Surgery, George Washington University School of Medicine and Health Sciences, Washington, DC
[16] Laboratory of Pathology, Center for Cancer Research, National Cancer Institute (NCI), NIH, Bethesda, MD
[17] Lymphoid Malignancies Branch, Center for Cancer Research, NCI, NIH, Bethesda, MD
[18] Lymphocyte Biology Section, LISB, NIAID, NIH, Bethesda, MD
[19] Program in Computational Biology and Bioinformatics, Yale University, New Haven, CT
[20] Department of Immunobiology, Yale School of Medicine, New Haven, CT
# These authors contributed equally
* Correspondence should be addressed to kalpana.manthiram@nih.gov and pams@nih.gov

Abstract

SARS-CoV-2 infection triggers adaptive immune responses from both T and B cells. However, most studies focus on peripheral blood, which may not fully reflect immune responses in lymphoid tissues at the site of infection. To evaluate both local and systemic adaptive immune responses to SARS-CoV-2, we collected peripheral blood, tonsils, and adenoids from 110 children undergoing tonsillectomy/adenoidectomy during the COVID-19 pandemic and found 24 with evidence of prior SARS-CoV-2 infection, including detectable neutralizing antibodies against multiple viral variants. We identified SARS-CoV-2-specific germinal center (GC) and memory B cells; single cell BCR sequencing showed that these virus-specific B cells were class-switched and somatically hypermutated, with overlapping clones in the adenoids and tonsils. Oropharyngeal tissues from COVID-19-convalescent children showed persistent expansion of GC and anti-viral lymphocyte populations associated with an IFN-γ-type response, with particularly prominent changes in the adenoids, as well as evidence of persistent viral RNA in both tonsil and adenoid tissues of many participants. Our results show robust, tissue-specific adaptive immune responses to SARS-CoV-2 in the upper respiratory tract of children weeks to months after acute infection, providing evidence of persistent localized immunity to this respiratory virus.

Introduction

SARS-CoV-2 induces humoral and cellular immune responses in children, primarily noted by assessing antibody and T cell responses in the peripheral blood[1,2]. However, little is known about immune responses to the virus in the lymphoid tissue of the upper respiratory tract where initial infection and viral replication take place[3,4]. The palatine tonsils and adenoids are secondary lymphoid structures at the mucosal surface of the naso- and oropharynx, where tissue-specific T and B cell responses to antigens in the upper respiratory tract can be generated[5,6]. Here, collaborative interactions between T follicular helper cells (Tfh) and B cells enable immunoglobulin gene class switching and formation of germinal centers (GCs), where B cells undergo somatic hypermutation of immunoglobulin genes that supports affinity maturation, resulting in the production of high-affinity antibodies and memory B cells. In adults with fatal COVID-19, loss of GCs in draining thoracic lymph nodes and consequentially, poor serum antibody durability have been reported; however, recently, others have found evidence of durable B cell responses derived from GCs including long-lived plasma cells in the bone marrow of convalescent adults as well as antigen-specific GC B cells and Tfh cells in the lymph nodes and lung tissues of organ donors[7-13]. As tonsillectomy and adenoidectomy are among the most common ambulatory surgeries in children, the tonsils and adenoids offer an accessible secondary lymphoid tissue enabling the study of GC and T cell responses to SARS-CoV-2 in children[14]. Using in-depth immune profiling, we characterized adaptive immune responses to SARS-CoV-2 in the tonsils and adenoids of convalescent children and described long-term alterations in tissue-specific B and T lymphocyte populations involved in GC and anti-viral memory responses following COVID-19.

87

Robust GC responses in pharyngeal lymphoid tissue

We collected blood, tonsils, and adenoids from 110 children who underwent tonsillectomy and/or adenoidectomy primarily from September 2020 to January 2021 (Fig. 1a, participant characteristics in Supplementary Tables 1-3). All participants were required to have a negative PCR for SARS-CoV-2 from a nasopharyngeal swab within 72 hours prior to surgery. Eleven participants had histories of confirmed SARS-CoV-2 infection by PCR or antigen detection from previous nasopharyngeal swabs, ranging from 25 to 303 days prior to surgery (average 102 days); 64% (7/11) of these participants reported symptoms at the time of positive testing (Fig. 1b, Supplementary Table 3). Thirteen additional participants with previous SARS-CoV-2 infection were identified after sample collection through serological testing and/or identification of B cells that bind probes for both the S1 domain of the spike protein (S1) and spike receptor binding domain (RBD) from SARS-CoV-2 (S1$^+$RBD$^+$), yielding a total of 24 participants with evidence of prior COVID-19 in our cohort (Fig. 1a, Supplementary Table 4). Neutralizing antibodies against the WA-1, B.1.1.7 (alpha), and B.1.429 (epsilon) strains were detected in the serum of all seropositive subjects but not in controls (Fig. 1c, Supplementary Table 4). Most seropositive subjects also had neutralizing antibodies to other strains including B.1.617.2 (delta), although fewer (9 out of 23) had neutralizing antibodies to B.1.1.529 (omicron) (Fig. 1c, Supplementary Table 4). Neutralizing titers were highest against the WA-1 strain and inversely correlated with time since positive PCR/antigen test in those participants with prior testing (Fig. 1d).

108

109   In nearly all seropositive participants, we detected S1$^+$RBD$^+$ B cells in PBMCs and both

110   pharyngeal tissues (Fig. 1e), with the exception of two donors (CNMC 91 and 104) who

111   had almost no S1$^+$RBD$^+$ binding B cells in the peripheral blood (Extended Data Fig. 1a).

112   These two donors also had the lowest serum neutralizing antibody titers to WA-1 among

113   our cohort. Surprisingly, one participant (CNMC 32) had high serum neutralization titers

114   but very low percentages of S1$^+$RBD$^+$ B cells, particularly in the oropharyngeal tissues,

115   highlighting heterogeneity in responses to SARS-CoV-2.

116

117   Evaluation of B cell populations by high-dimensional flow cytometry revealed that the

118   majority of S1$^+$RBD$^+$ B cells were CD27$^+$ immunoglobulin (Ig) class-switched memory B

119   cells (IgD$^-$CD38$^-$CD27$^+$) (Fig. 1f-g, Extended Data Fig. 1b, Supplementary Fig. 1-2),

120   indicating a robust memory B cell response was generated and maintained in the upper

121   respiratory tract as long as 10 months into the convalescent period (Extended Data Fig.

122   1c). These S1$^+$RBD$^+$ memory B cells were primarily IgG$^+$, with lower percentages of IgA$^+$

123   cells compared to total CD27$^+$ memory B cells in the tissue, perhaps reflecting the

124   inflammatory milieu during infection (Extended Data Fig. 1d). Of note, the percentage of

125   S1$^+$RBD$^+$ cells we found among CD27$^+$ switched memory B cells in the oropharyngeal

126   tissue was comparable to that recently reported in lung and lung-draining lymph nodes

127   from convalescent autopsy donors (Fig. 1f, Extended Data Fig. 1e)[13].

128

129   The predominance of Ig class-switched CD27$^+$ memory B cells among S1$^+$RBD$^+$ B cells

130   suggested that they originated from GC reactions, although the timing of class switching

131   remains controversial[15]. Because the tonsils and adenoids are secondary lymphoid tissues

132 and sites of robust GC formation, we could directly examine the involvement of GCs. Flow

133 cytometric analysis revealed a substantial portion of GC B cells among the $S1^+RBD^+$ B

134 cells in both tissues (Fig. 1g). Paired analyses of tonsils and adenoids from the same donor

135 revealed that the adenoids had higher frequencies of $S1^+RBD^+$ cells among both total and

136 GC B cells compared to tonsils, perhaps reflecting higher viral exposure due to their

137 location in the nasopharynx (Extended Data Fig. 1f-g). Frequencies of $S1^+RBD^+$ B cells in

138 the adenoids, but not tonsils or PBMCs, correlated significantly with serum neutralization

139 titers for B.1.351 (beta), B.1.526 (iota), B.1.617.2 (delta), and B.1.1.529 (omicron) variants,

140 further highlighting the importance of the adenoids in generating immune responses to

141 SARS-CoV-2 (Extended Data Fig. 1h). Furthermore, in contrast to previous reports of

142 absent GC structures in secondary lymphoid organs in postmortem analyses of adults who

143 died from severe COVID-19[7], we observed intact GC structures in both adenoid and tonsil

144 tissue of children following COVID-19 using multiplex immunofluorescence microscopy,

145 with discrete dark and light zones; COVID-19-convalescent tissues did not exhibit smaller

146 or fewer GCs relative to tissues from uninfected controls (Fig. 1h; Extended Data Fig. 1i-j).

147

148 Early responses to SARS-CoV-2 in symptomatic patients have been shown to be

149 dominated by extrafollicular responses, characterized by expansion of IgD^-CD27^- double

150 negative (DN, $IgD^-CD27^-CD38^-CD19^+$) B cells[16,17]. We also saw an expansion of DN B

151 cells among $S1^+RBD^+$ B cells in both adenoids and tonsils (Fig. 1g). However, most of

152 these $S1^+RBD^+$ DN B cells exhibited characteristics of DN1 ($CD21^+CD11c^-$) cells, which

153 are derived from GCs (Fig. 1i). Only a small portion were DN2 ($CD21^-CD11c^+$) cells, which

154 originate from extrafollicular B cell activation and were reported to expand in acute severe

155 COVID-19[16]. Our findings, therefore, suggest that robust humoral responses to SARS-

156 CoV-2 associated with intact GC reactions and B cell memory are present in the upper

157 respiratory tract mucosal lymphoid tissue.

158

159 **Multimodal single-cell analysis of SARS-CoV-2-specific B cells**

160 To investigate B cell responses in greater detail, we sorted S1-binding (S1$^+$) and non-

161 binding (S1$^-$) B cells from tonsils, adenoids, and PBMCs from two subjects with a history

162 of COVID-19, as well as one uninfected control (Supplementary Fig. 3a-b). Over 1860 S1$^+$

163 B cells and 25000 S1$^-$ B cells were captured and characterized by CITE-seq (Cellular

164 Indexing of Transcriptomes and Epitopes by Sequencing), which simultaneously measured

165 the expression of 22 B cell surface markers and sequenced the transcriptome and

166 V(D)J/BCR in single cells. We performed unsupervised clustering using cell surface protein

167 expression profiles (Fig. 2a-d, Extended Data Fig. 2a) and assessed the expression of

168 memory B cell, GC B cell, and plasma cell/plasmablast transcriptional signatures in each

169 cluster[18] (Fig. 2e, Extended Data Fig. 2b). Surface antibody staining patterns were

170 concordant with the cell types suggested by the gene expression signatures in each cluster

171 (S1$^+$ B cells in Fig. 2e, total B cells in Extended Data Fig. 2a-b). Consistent with our flow

172 cytometric analysis, the majority of S1$^+$ B cells in the tonsils and adenoids were in cluster

173 2, which represented CD27$^+$ memory B cells (Fig. 2c-e). Adenoids and tonsils had a smaller

174 but clear portion of S1$^+$ cells that were in cluster 4, which had a GC B cell gene expression

175 signature and surface protein profile (Fig. 2b-e, Extended Data Fig. 2a-b). In contrast, S1$^+$

176 cells in the blood were primarily in cluster 9 (Fig. 2a-c, e), which was also a CD27$^+$IgD$^-$

177 population (Fig. 2e, lower heatmap) but had different surface marker and gene expression

178 profiles compared to CD27+IgD- memory B cells in the lymphoid tissues (Fig. 2e, upper

179 heatmap; Extended Data Fig. 2a). S1+ cells from both the peripheral blood and tissues also

180 clustered separately when cells were clustered by transcript expression alone (Extended

181 Data Fig. 3). Furthermore, S1+ memory B cells in cluster 2 had higher expression of *CXCR3*

182 and *HOPX*, genes known to be induced by T-bet in T cells[19], than their S1- counterparts,

183 suggesting that they may have developed in a more IFN-γ rich environment

184 (Supplementary Table 5, Extended Data Fig. 2c). These S1+ memory B cells also had

185 decreased expression of several regulatory receptors that inhibit BCR signaling including

186 *FCGR2B, FCRL2, FCRL3,* and *TNFRSF13B* (encoding TACI)[20,21] (Supplementary Table

187 5, Extended Data Fig. 2c).

188

189 BCR sequence analysis confirmed that S1+ B cells were primarily IgG1 and IgA1 class-

190 switched cells (Fig. 3a, Extended Data Fig. 2d), with high frequencies of somatic

191 hypermutation (SHM) in V_H genes (Fig. 3b, Extended Data Fig. 2e) and low clonal diversity

192 compared to S1- B cells, indicative of antigen-driven clonal expansion (Fig. 3c). The high

193 mutation frequency in S1+ B cells is consistent with prior work showing that subjects with

194 mild COVID-19 had higher frequencies of hypermutated memory B cells compared to those

195 with severe COVID-19[22] and suggests that these SARS-CoV-2-specific clones underwent

196 somatic hypermutation in GCs.

197

198 Intriguingly, we also observed that a portion of S1+ B cell clones (a total of 83 cells from 29

199 clones: 20 clones from donor 89 and 9 from donor 71) were present in both the tonsils and

200 adenoids (Fig. 3d). The shared S1+ clones were nearly all isotype-switched cells (Extended

201 Data Fig. 2f) and, like the total S1$^+$ B cell population, were comprised primarily of cells from

202 cluster 2 (CD27$^+$ memory B cells) (Fig. 2e). However, a small number of cells from shared

203 clones in the tonsil of one donor were GC B cells (cluster 4) (Fig. 2e; Supplementary Table

204 6). The distribution of these shared clones across adenoid and tonsil within some clonal

205 lineage trees suggested that B cell clones migrated between these oropharyngeal lymphoid

206 tissues and raised the possibility that class switching can occur before, during, or after

207 SHM (Fig. 3e). Thus, multimodal single cell analysis of the SARS-CoV-2-specific B cells

208 both supports their emergence from GCs and suggests sharing and potential migration of

209 clonally expanded B cells between oropharyngeal lymphoid tissues.

210

211 **Expanded GC populations after COVID-19**

212 To determine whether prior SARS-CoV-2 infection can broadly alter the immune landscape

213 of mucosal tissues beyond acute infection, we compared the immune cell profiles of tonsils,

214 adenoids, and peripheral blood from individuals with a history of COVID-19 to those

215 without, using both unsupervised analyses and manual gating of high-dimensional flow

216 cytometry data (samples included in each analysis are listed in Supplementary Table 2).

217 To probe cell populations in greater detail, CD19$^+$ B, CD4$^+$ T, and CD8$^+$ T lymphocytes

218 were first gated and then analyzed separately. Adenoids and tonsils were evaluated

219 together, whereas PBMCs were examined on their own, to account for and increase

220 sensitivity for detecting distinct populations in tissues and peripheral blood.

221

222 In the unsupervised analysis of B cell phenotypes, we compared those with prior COVID-

223 19 to control subjects while controlling for age and sex. This analysis highlighted 14

224   clusters and revealed more pronounced changes in the adenoids post-COVID-19 (Fig. 4a-

225   b, Extended Data Fig. 4). Clusters 3 and 10 were significantly increased in the adenoids of

226   participants with a history of COVID-19 (Fig. 4b); these clusters represented IgG$^+$ and IgM$^+$

227   GC B cells, respectively. In addition, cluster 14, which clustered with naïve B cells, was

228   decreased in both adenoids and tonsils of COVID-19 convalescent subjects (Fig. 4a-b). In

229   the peripheral blood, a CD127$^+$IgD$^+$ B cell cluster was also decreased following COVID-19

230   (Fig. 4c-d, Supplementary Fig. 4a-b); this was confirmed by manual gating on CD127$^+$ B

231   cells (Fig. 4e). Thus, prior COVID-19 is associated with prolonged changes in B cell

232   populations well into convalescence, including persistent enrichment of GC B cells in the

233   adenoids.

234

235   **Expanded Tfh populations after COVID-19**

236   Post-COVID-19, we observed that the adenoids had lower percentages of CD4$^+$ T cells

237   (Extended Data Fig. 5a). Unsupervised clustering further underscored differences in

238   COVID-19-convalescent samples (Fig. 5a-b, Extended Data Fig. 6a-b) that included a

239   reduction in cluster 9, which represents naïve CD4$^+$ T cells (CD45RA$^+$CCR7$^+$), in both

240   tonsils and adenoids from COVID-19 convalescent subjects (Fig. 5a-b). Traditional gating

241   confirmed decreased percentages of naïve CD4$^+$ T cells in lymphoid tissue (Fig. 5c).

242

243   Conversely, cluster 3, which represents a CD57$^+$PD-1^{hi} subset, was significantly enriched

244   after COVID-19 in both the adenoids and tonsils (Fig. 5a-b); manual gating confirmed an

245   expanded CD57$^+$PD-1^{hi} CD4$^+$ T cell population in the tissues (Fig. 5d). CD57 has been

246   described as a marker of T cell senescence but is also found on a population of tonsillar

247   GC-Tfh cells[23-25], a subset of CD4$^+$ T helper cells that provide contact-mediated signals to

248   antigen-stimulated B cells for GC formation and maintenance. Compared to the total CD4$^+$

249   T cell population in the tissues, the CD57$^+$PD-1^{hi} CD4$^+$ T cell population exhibited higher

250   expression of CXCR5 and CD69, indicative of a Tfh phenotype and characteristic of tissue-

251   resident memory T (TRM) cells, respectively[6] (Fig. 5e). Imaging studies revealed that

252   CD57$^+$PD-1^{hi} CD4$^+$ T cells were located within the GC (Fig. 5f). Moreover, their frequency

253   positively correlated with the proportion of GC B cells in both the adenoids and tonsils

254   (Extended Data Fig. 5b-c). The percentage of cluster 3 also positively correlated with the

255   percentage of S1$^+$RBD$^+$ B cells that were GC B cells in the adenoids (Extended Data Fig.

256   5d), supporting the idea that these T cells contributed to the generation and persistence of

257   SARS-CoV-2-specific GC responses. Consistent with these data, stimulation with PMA

258   and ionomycin showed that CD57$^+$PD-1^{hi} CD4$^+$ T cells from the adenoids and tonsils

259   produced IL-21 and IL-10, cytokines that facilitate GC formation and B cell antibody

260   secretion (Extended Data Fig. 5e-f).

261

262   Cluster 6 was also significantly increased in COVID-19-convalescent subjects but only in

263   the adenoids (Fig. 5a-b, Extended Data Fig. 5g). This cluster represented a pre-Tfh cell

264   population (CD45RA$^-$CXCR5$^+$PD-1^{int}) that expressed CXCR3 but not CCR6 (Extended

265   Data Fig. 6a-b), a combination of markers associated with IFN-γ/Th1 cytokine production[26].

266   Upon PMA and ionomycin stimulation, a high percentage of CXCR3$^+$CCR6$^-$ pre-Tfh cells

267   produced IFN-γ (Extended Data Fig. 5h), suggesting that type 1 (IFN-γ-associated) T cell

268   responses were induced as part of the anti-viral response to SARS-CoV-2 in the adenoids.

269

270   To further evaluate T cell function, we examined the overall patterns of cytokine production

271   from tonsil and adenoid cells stimulated with PMA and ionomycin. Global evaluation of

272   CD4$^+$ T cell polyfunctionality by SPICE (Simplified Presentation of Incredibly Complex

273   Evaluations) revealed several combinations of cytokines were significantly enriched in the

274   post-COVID-19 group (Fig. 5g, Supplementary Fig. 6); two of these combinations included

275   IL-21 (categories 33 and 41), suggesting production by Tfh cells. One of the enriched

276   combinations included IL-10 in addition to IL-21; IL-10 production by Tfh cells is important

277   for maintaining GCs in viral infections[27] and is expressed by CD57+ Tfh cells. Notably,

278   increased IFN-γ was also part of a cytokine pattern (category 27) specifically enriched in

279   adenoids post-COVID-19, perhaps reflecting the increased CXCR3$^+$CCR6$^-$ pre-Tfh

280   population (cluster 6) we observed. Consistent with this, we find more robust IFN-γ

281   production by CD4$^+$ T cells in adenoids compared to the tonsils indicating inherent

282   differences in the T cell populations in these lymphoid tissues (Extended Data Fig. 5i).

283

284   Finally, in accordance with evidence of robust GC responses in the adenoids and tonsils

285   post-COVID-19, we found more T follicular regulatory (Tfr) cells (CXCR5$^+$PD-1^{hi}) among

286   CD127$^-$CD25$^+$ regulatory T cells in COVID-19-convalescent tonsils and adenoids (Fig. 5h);

287   the frequency of these cells positively correlated with the percentage of GC B cells

288   (Extended Data Fig. 5j-k). Similar to the characteristics we found in adenoid CD4$^+$ T cells,

289   regulatory T cells (CD25$^+$CD127$^-$) in the adenoids were also more activated after COVID-

290   19, with a higher percentage of HLA-DR$^+$CD38$^+$ and CXCR3$^+$CCR6$^-$ cells, again

291   suggesting the adenoids may have been primed by a stronger immune response to SARS-

292   CoV-2 than the tonsils (Extended Data Fig. 5l-m). Thus, we find an expansion of

293 percentages of Tfh as well as Tfr cells in the tonsils and adenoids that extends into

294 convalescence, providing further evidence for prolonged GC responses to SARS-CoV-2 in

295 the upper respiratory tract of children.

296

297 **Enrichment of activated circulating Tfh cells in the blood following COVID-19**

298 Because lymphocyte populations in the peripheral blood differ from the tonsil and adenoid,

299 we evaluated PBMCs separately; unsupervised grouping of high-dimensional flow

300 cytometry data revealed two clusters (cluster 5 and cluster 11) that were increased

301 following COVID-19 (Fig. 6a-b, Supplementary Fig. 7a-b); both contained circulating Tfh

302 (cTfh)-like cells (CD45RA$^-$CXCR5$^+$PD-1$^+$) that expressed CD38, a marker of recently

303 activated T cells[28]; cluster 11 was CXCR3$^+$ while cluster 5 was not. Although we did not

304 find increased percentages of total cTfh cells by manual gating, we found that cTfh cells

305 were skewed to a CXCR3$^+$CCR6$^-$ phenotype in the COVID-19-experienced group (Fig. 6c);

306 these cells produced IFN-γ upon stimulation with PMA and ionomycin (Extended Data Fig.

307 7a). Analogous to prior reports, we also observed an increased frequency of stem cell-like

308 memory CD4$^+$ T (T$_{SCM}$) (CD45RA$^+$CCR7$^+$CD28$^+$CD27$^+$CD95$^+$) (Extended Data Fig. 7b),

309 perhaps reflecting long-lived memory T cells following recovery from COVID-19 in

310 children[29].

311

312 To identify SARS-CoV-2 antigen-specific CD4$^+$ T cells, we stimulated tonsil, adenoid, and

313 peripheral blood mononuclear cells with spike (S), membrane (M), and nucleocapsid (N)

314 peptide pools and assessed the activation-induced markers (AIM) CD40L, OX40, and 4-

315 1BB on T cells. Although we were not able to precisely identify and phenotype the SARS-

316 CoV-2-specific T cells in the adenoids and tonsils due to the highly activated status of T

317 cells at baseline without stimulation in these tissues (Extended Data Fig. 7c-d), SARS-

318 CoV-2-reactive CD4$^+$ T cells were identified in the peripheral blood with the greatest

319 responses to the S peptide pool (Fig. 6d-e). By concatenating all the peptide-activated

320 CD4$^+$ T cells, we found that the SARS-CoV-2-responsive CD4$^+$ T cells in the peripheral

321 blood were primarily memory cells that were enriched for CXCR3$^+$ cTfh cells (CD45RA$^-$

322 CXCR5$^+$PD-1$^+$) and expressed high levels of HLA-DR, CD38, and ICOS (Fig. 6f, Extended

323 Data Fig. 7e). This enrichment of CXCR3$^+$ cTfh-like cells in the peripheral blood, a portion

324 of which are SARS-CoV-2-specific, likely parallels the skewing of pre-Tfh cells we found in

325 the pharyngeal lymphoid tissue in response to SARS-CoV-2.

326

327 **Expanded tissue resident CD8$^+$ cells after COVID-19**

328 To further evaluate anti-viral responses, we examined CD8$^+$ T cell in the tonsils and

329 adenoids. With unsupervised clustering, we found that cluster 1, which represented naïve

330 CD8$^+$ T cells, decreased following COVID-19 in the adenoids (Fig. 7a-b, Extended Data

331 Fig. 8a-b; Extended Data Fig. 9a); manual gating revealed a similar, but not significant

332 trend in both adenoids and tonsils, in addition to more effector memory CD8$^+$ T cells in the

333 tonsils of the COVID-19 experienced cohort (Extended Data Fig. 9b-c). Although not

334 statistically significant, both adenoids and tonsils exhibited increases in cluster 2 and

335 cluster 3 following COVID-19. These two clusters represented activated effector memory

336 CD8$^+$ T cells (HLA-DR$^+$CD38$^+$CXCR3$^+$CCR7$^-$CD45RA$^-$); cluster 2 expressed higher CD38,

337 while cluster 3 expressed more CD57. Manual gating demonstrated that CD57$^+$PD-1$^+$ CD8$^+$

338 T cells were significantly higher in adenoids and tonsils (Fig. 7c), while activated HLA-

339   DR+CD38+ CD8+ T cells trended higher in tonsils of the COVID-19-convalescent group

340   (Extended Data Fig. 9d). As in CD4+ T cells, the COVID-19-convalescent adenoids also

341   had significantly more CXCR3+CCR6- CD8+ T cells (Tc1 skewed) (Extended Data Fig. 9e).

342   Furthermore, CD8+ T cells in the adenoid produced more IFN-γ than those in the tonsils

343   upon PMA/ionomycin stimulation, again indicating the ability of the adenoids to create a

344   more IFN-γ rich environment during the anti-viral response (Extended Data Fig. 9f).

345

346   CD8+ T cells expressing the senescence marker CD57 and inhibitory surface protein PD-

347   1 are expanded in the peripheral blood of adults with moderate and severe COVID-19;

348   however, the function of these cells and whether they represent a non-functional

349   "exhausted" population is not clear[30,31]. We found that CD57+PD-1+ CD8+ T cells in the

350   adenoids and tonsils had robust pro-inflammatory cytokine and cytotoxic factor production

351   following PMA and ionomycin stimulation (Extended Data Fig. 9g-h).

352

353   Further analysis of both CD57+PD-1+CD8+ T cells in the tissue showed that the vast

354   majority expressed the tissue-resident markers CD103 and CD69 in addition to CXCR5

355   (Fig. 7d) and these cells were found in the GC (Fig. 7e). HLA-DR+CD38+ CD8+ T cells also

356   expressed CD103, CD69, and CXCR5 (Extended Data Fig. 9i). CXCR5+CD8+ T cells in

357   lymphoid tissue have been shown to resemble stem-like or progenitor cells that maintain

358   anti-viral function in chronic viral infections[32-37]. The role of these cells in the cellular

359   immune response to an acute respiratory virus like SARS-CoV-2 is unknown, but their

360   expansion and location in the GC raises questions about their roles in GCs and other anti-

361   viral responses. In line with the expansion of activated CD8+ T cells in these tissues,

362   evaluation of global cytokine production from CD8$^+$ T cells by SPICE revealed multiple

363   combinations of cytokines and cytotoxic molecules were significantly enriched post-

364   COVID-19, most notably in the tonsils (Fig. 7f, Supplementary Fig. 9). Thus, activated CD8$^+$

365   T cell populations were enriched in the pharyngeal lymphoid tissues post-COVID-19.

366

367   In contrast, we did not find significant differences in CD8$^+$ T cells in the PBMCs (Extended

368   Data Fig. 10a-b, Supplementary Fig. 10a-b), with the exception of more abundant CD8$^+$

369   T$_{SCM}$ cells (CD45RA$^+$CCR7$^+$CD28$^+$CD27$^+$CD95$^+$) seen by manual gating of COVID-19-

370   convalescent samples (Extended Data Fig. 10c), parallel to our findings in peripheral CD4$^+$

371   T cells and perhaps reflecting long-lived memory populations.

372

373   Together, these results provide evidence of activated and cytotoxic CD8$^+$ TRM cells

374   associated with increased cytokine production and GC localization in the pharyngeal

375   lymphoid tissue, suggesting longer lasting effects of prior infection on these tissues

376   compared to peripheral blood in convalescence. Thus, the pharyngeal lymphoid tissues

377   may provide a unique window into the prolonged effects of SARS-CoV-2 infection.

378

379   **Viral RNA persistence in the pharyngeal tissue**

380   Given the apparent prolonged immune activation we observed in the pharyngeal tissue of

381   children post-SARS-CoV-2 infection, we evaluated these tissues for evidence of viral

382   persistence. RNA isolated from formalin-fixed, paraffin-embedded (FFPE) samples of

383   tonsils and adenoids were analyzed by digital droplet PCR (ddPCR) for evidence of SARS-

384   CoV-2 nucleocapsid RNA (N1 and N2). Viral RNA was found in multiple samples of COVID-

385   19-convalescent tissues, despite negative PCRs from nasopharyngeal swabs at the time

386   of surgery (Fig. 8a, Supplementary Table 7). SARS-CoV-2 was detected in 7 out of 9 FFPE

387   adenoid blocks and 15 out of 22 FFPE tonsil blocks from COVID-19-convalescent

388   individuals, but not in any control tissue samples. In several samples, participants' previous

389   positive PCR from a nasal swab was over 100 days prior to surgery, including one which

390   was 303 days before surgery. Moreover, the copies of viral RNA significantly correlated

391   with the percentage of $S1^+RBD^+$ cells among GC B cells in the tonsil (Fig. 8b). Although

392   SARS-CoV-2 RNA was found in only a subset of post-COVID-19 tissues and we were

393   unable to detect viral protein, these results raise the question of whether antigen

394   persistence contributes to the prolonged lymphoid and GC responses we found following

395   COVID-19.

396

397   **Discussion**

398   Analysis of the tonsils and adenoids offers a unique opportunity to evaluate immune

399   responses to a novel respiratory virus at the primary site of infection. Here, we demonstrate

400   (1) direct evidence of robust SARS-CoV-2 antigen-specific GC and memory B cell

401   responses in the upper respiratory tract lymphoid tissues post-COVID-19; (2) the presence

402   of overlapping S1-reactive B cell clones in the tonsils and adenoids highlighting the

403   dynamic nature of these anti-viral responses, (3) long-lasting expansion of cells involved

404   in GC and anti-viral responses, including GC B, Tfh, Tfr, and effector $CD8^+$ TRM cells in

405   the lymphoid tissues and cTfh1 cells in the peripheral blood, (4) type 1 (IFN-γ-associated)

406   skewing with $CXCR3^+$ T lymphocytes, particularly in the adenoids, with corresponding

407   changes in antigen-specific memory B cells, and (5) persistence of SARS-CoV-2 RNA in

408   the lymphoid tissues months after infection. Together, these results demonstrate ongoing,

409   tissue-specific immune responses to SARS-CoV-2 in oropharyngeal lymphoid tissues of

410   children in the convalescent phase.

411

412   We identified 24 children out of 110 with evidence of prior COVID-19, most of whom were

413   unaware of their infection status and/or asymptomatic. We note that these samples were

414   taken prior to the availability of vaccination for children and thus reflected true infection.

415   The high percentage of positive children during this period of collection, ending in early

416   2021, is notable and underscores the extent of infection present in this urban

417   population[38,39]. In most of our pediatric participants, we found SARS-CoV-2-specific

418   memory B cells in the peripheral blood and oropharyngeal tissue, indicating sustained

419   humoral memory in both the local tissue and blood. Nonetheless, a few participants had

420   low frequencies of memory B cells in the peripheral blood and/or oropharyngeal tissue

421   and/or low serum neutralizing antibody titers, reflecting heterogeneous responses that may

422   leave some children prone to repeat infection.

423

424   Other groups have noted lasting changes in the T and B cell populations in the peripheral

425   blood of adults months after COVID-19[40-42]; a recent analysis of immune cells in the nasal

426   mucosa also revealed enrichment of activated $CD38^+CD8^+$ TRM and $CD127^+$ granulocytes

427   weeks after acute infection[43]. In our analysis of both upper respiratory tissue and peripheral

428   blood, we see prominent changes in tonsils and adenoids compared to peripheral blood,

429   providing evidence for tissue-specific anti-viral immune responses. Moreover, many of the

430   enriched B and T cell populations we found in the pharyngeal tissue are functional tissue-

431 resident populations involved in GC development and anti-viral responses that likely

432 remain at the primary site of infection for months and even years, poised to provide

433 localized immune protection[44]. These expanded tissue-resident T cell populations,

434 including pre-Tfh and CD8^{+} TRM, exhibit type 1 skewing and may have created an IFN-γ-

435 rich environment that led to upregulation of *CXCR3* and *HOPX* among S1^{+} B cells in the

436 tissue. Strong local IFN (Type I and Type II) responses were recently found in the upper

437 airways of infected children and likely led to enhanced viral control and milder disease

438 compared to adults[45,46]. Here, we provide evidence for prolonged IFN-γ-induced responses

439 in convalescent children. Whether immunization also generates immunity to SARS-CoV-2

440 in the upper respiratory tract and how this compares to natural infection are important

441 questions that may have implications for determining optimal routes of vaccination.

442

443 Among the pharyngeal tissues we evaluated, the adenoids sustained more significant

444 changes following COVID-19 than the tonsils; the frequency of SARS-CoV-2 specific B

445 cells in the adenoids also correlated strongly with serum neutralizing titers for several

446 variants including omicron providing evidence for the key role of this lymphoid tissue in

447 anti-viral responses. Although they are both pharyngeal mucosal tissues, the adenoids and

448 palatine tonsils differ in a number of ways. The adenoids are in the nasopharynx and have

449 a respiratory epithelium, while the palatine tonsils are in the oropharynx and have a

450 stratified squamous epithelium. We also found that T cells in the adenoid can produce more

451 IFN-γ. These, as well as differences in the other immune cell populations, may make the

452 adenoids more susceptible to immune activation during infection with a respiratory virus

453 like SARS-CoV-2 than the tonsils. Although the adenoids are only one of many lymphoid

454   structures in the upper respiratory tract with likely redundant function in generating an

455   immune response to respiratory viruses, our data trigger questions as to whether

456   adenoidectomy and tonsillectomy affect immune responses to SARS-CoV-2.

457

458   Longitudinal studies of SARS-CoV-2-specific B cells suggest continued maturation in GCs

459   months after infection with peripheral memory B cell clones acquiring greater somatic

460   hypermutation with time, possibly due to persistence of antigen in the tissue[17,41,47].

461   Maintenance of SARS-CoV-2-specific GC B cells and Tfh cells has also been noted in lung

462   and lung-associated lymph nodes of 4 organ donors; in one case, this was observed at

463   least 6 months following infection[13]. Using tissues from tonsillectomies and

464   adenoidectomies, we were able to directly query lymphoid tissue at the primary site of

465   infection in the upper respiratory tract and find compelling evidence of ongoing SARS-CoV-

466   2-specific GC reactions with Tfh and effector memory CD8$^+$ T cell expansion, perhaps in

467   response to persistent viral antigen in the tissue months after the acute infection. Our

468   results suggest these tissues can provide a powerful tool for examining responses to

469   SARS-CoV-2.

470

471   Moreover, our observation of overlapping S1$^+$ B cells clones between tonsil and adenoid

472   tissue suggests that antigen-specific B cells may migrate between these tissues as part of

473   an ongoing immune response. B cells emerging from a single clone have been found

474   distributed among numerous Peyer's patches and intestinal lymph nodes and among upper

475   and lower respiratory tract tissues[48-50]. Our ability to query multiple tissues from the same

476   subject also reveals immunologic connections among the lymphoid tissues of the upper

477 respiratory tract. Additional analyses may help determine whether reseeding of germinal

478 centers and additional rounds of SHM occur in migrating B cell clones[51,52]; recent analyses

479 of B cell lineages following seasonal influenza vaccination provide a framework to test this

480 hypothesis[53]. Further work may also help determine whether persistence of antigen in the

481 tissue correlates with this B cell migration and evolution. The availability of tonsil and

482 adenoid tissues may facilitate such studies.

483

484 A limitation of our study is lack of information about the date of infection and presence of

485 symptoms in many participants due to their lack of awareness of having COVID-19. In

486 addition, we do not have longitudinal samples over time from participants to precisely map

487 the duration of immunologic changes; instead, we relied on time from positive PCR/antigen

488 testing to surgery as a proxy. We were also unable to clearly delineate antigen-specific T

489 cells in the tonsils and adenoids likely due to the activated nature of T cells in their

490 chronically inflamed environment. Given the increase in activated populations we observe,

491 it is possible that the expanded Tfh and CD8$^+$ T cells we found in the tissue may develop

492 in part as a result of bystander activation during the anti-viral response. Lastly, COVID-19-

493 convalescent participants underwent tonsillectomy for sleep disordered breathing or

494 obstructive sleep apnea due to hypertrophy of the adenoids and/or tonsils, which may be

495 an immunologic disorder[54]. Although control samples also came from individuals with the

496 same conditions, it is possible that these chronic disease states influence the immune

497 response to SARS-CoV-2.

498

499 Our findings offer insights into how viral infections may shape the mucosal immune tissue

500 in children beyond the acute phase of infection; maintenance of activated tissue-resident

501 T cells may affect responses against future infectious insults. These cells may also be

502 involved in pathologic responses. It is possible that enrichment of these activated cells in

503 the tissue into convalescence plays a role in delayed or prolonged sequelae of COVID-19

504 including multisystem inflammatory syndrome in children (MIS-C) or long-haul COVID-19.

505 Children with MIS-C have a high frequency of HLA-DR$^+$CD38$^+$ CD8$^+$ T cells and IFN-γ-

506 induced signatures in the peripheral blood and have mucocutaneous findings including

507 pharyngeal erythema, raising the question of whether type 1 skewed TRM cells may be

508 involved[55-57]. The repository of pharyngeal tissues we have generated may facilitate

509 evaluation of these and other important questions.

510 **Main References:**

511 1   Weisberg, S. P. *et al.* Distinct antibody responses to SARS-CoV-2 in children and
512   adults across the COVID-19 clinical spectrum. *Nature Immunology* **22**, 25-31,
513   doi:10.1038/s41590-020-00826-9 (2021).
514 2   Pierce, C. A. *et al.* Immune responses to SARS-CoV-2 infection in hospitalized
515   pediatric and adult patients. *Science Translational Medicine* **12**, eabd5487,
516   doi:10.1126/scitranslmed.abd5487 (2020).
517 3   Wölfel, R. *et al.* Virological assessment of hospitalized patients with COVID-2019.
518   *Nature* **581**, 465-469, doi:10.1038/s41586-020-2196-x (2020).
519 4   Huang, N. *et al.* SARS-CoV-2 infection of the oral cavity and saliva. *Nature*
520   *Medicine* **27**, 892-903, doi:10.1038/s41591-021-01296-8 (2021).
521 5   Wagar, L. E. *et al.* Modeling human adaptive immune responses with tonsil
522   organoids. *Nature Medicine* **27**, 125-135, doi:10.1038/s41591-020-01145-0
523   (2021).
524 6   Kumar, B. V. *et al.* Human Tissue-Resident Memory T Cells Are Defined by Core
525   Transcriptional and Functional Signatures in Lymphoid and Mucosal Sites. *Cell*
526   *Rep* **20**, 2921-2934, doi:10.1016/j.celrep.2017.08.078 (2017).
527 7   Kaneko, N. *et al.* Loss of Bcl-6-Expressing T Follicular Helper Cells and Germinal
528   Centers in COVID-19. *Cell* **183**, 143-157.e113, doi:10.1016/j.cell.2020.08.025
529   (2020).
530 8   Zhang, J. *et al.* Spike-specific circulating T follicular helper cell and cross-
531   neutralizing antibody responses in COVID-19-convalescent individuals. *Nature*
532   *Microbiology* **6**, 51-58, doi:10.1038/s41564-020-00824-5 (2021).

533   9   Wang, Z. *et al.* Naturally enhanced neutralizing breadth against SARS-CoV-2 one
534   year after infection. *Nature* **595**, 426-431, doi:10.1038/s41586-021-03696-9
535   (2021).
536   10   Turner, J. S. *et al.* SARS-CoV-2 infection induces long-lived bone marrow plasma
537   cells in humans. *Nature* **595**, 421-425, doi:10.1038/s41586-021-03647-4 (2021).
538   11   Zohar, T. *et al.* Compromised Humoral Functional Evolution Tracks with SARS-
539   CoV-2 Mortality. *Cell* **183**, 1508-1519.e1512, doi:10.1016/j.cell.2020.10.052
540   (2020).
541   12   Rydyznski Moderbacher, C. *et al.* Antigen-Specific Adaptive Immunity to SARS-
542   CoV-2 in Acute COVID-19 and Associations with Age and Disease Severity. *Cell*
543   **183**, 996-1012.e1019, doi:10.1016/j.cell.2020.09.038 (2020).
544   13   Poon, M. M. L. *et al.* SARS-CoV-2 infection generates tissue-localized
545   immunological memory in humans. *Science Immunology* **0**, eabl9105,
546   doi:doi:10.1126/sciimmunol.abl9105.
547   14   Mitchell, R. B. *et al.* Clinical Practice Guideline: Tonsillectomy in Children
548   (Update). *Otolaryngol Head Neck Surg* **160**, S1-s42,
549   doi:10.1177/0194599818801757 (2019).
550   15   Roco, J. A. *et al.* Class-Switch Recombination Occurs Infrequently in Germinal
551   Centers. *Immunity* **51**, 337-350.e337, doi:10.1016/j.immuni.2019.07.001 (2019).
552   16   Woodruff, M. C. *et al.* Extrafollicular B cell responses correlate with neutralizing
553   antibodies and morbidity in COVID-19. *Nature Immunology* **21**, 1506-1516,
554   doi:10.1038/s41590-020-00814-z (2020).
555   17   Sokal, A. *et al.* Maturation and persistence of the anti-SARS-CoV-2 memory B cell
556   response. *Cell* **184**, 1201-1213.e1214, doi:10.1016/j.cell.2021.01.050 (2021).
557   18   Milpied, P. *et al.* Human germinal center transcriptional programs are de-
558   synchronized in B cell lymphoma. *Nature Immunology* **19**, 1013-1024,
559   doi:10.1038/s41590-018-0181-4 (2018).
560   19   Albrecht, I. *et al.* Persistence of effector memory Th1 cells is regulated by Hopx.
561   *Eur J Immunol* **40**, 2993-3006, doi:10.1002/eji.201040936 (2010).
562   20   Jackson, T. A., Haga, C. L., Ehrhardt, G. R. A., Davis, R. S. & Cooper, M. D. FcR-
563   like 2 Inhibition of B cell receptor-mediated activation of B cells. *J Immunol* **185**,
564   7405-7412, doi:10.4049/jimmunol.1002305 (2010).
565   21   Ben Mkaddem, S., Benhamou, M. & Monteiro, R. C. Understanding Fc Receptor
566   Involvement in Inflammatory Diseases: From Mechanisms to New Therapeutic
567   Tools. *Frontiers in Immunology* **10**, doi:10.3389/fimmu.2019.00811 (2019).
568   22   Hoehn, K. B. *et al.* Cutting Edge: Distinct B Cell Repertoires Characterize Patients
569   with Mild and Severe COVID-19. *The Journal of Immunology*, ji2100135,
570   doi:10.4049/jimmunol.2100135 (2021).
571   23   Brenchley, J. M. *et al.* Expression of CD57 defines replicative senescence and
572   antigen-induced apoptotic death of CD8+ T cells. *Blood* **101**, 2711-2720,
573   doi:10.1182/blood-2002-07-2103 (2003).
574   24   Alshekaili, J. *et al.* STAT3 regulates cytotoxicity of human CD57+ CD4+ T cells in
575   blood and lymphoid follicles. *Sci Rep* **8**, 3529, doi:10.1038/s41598-018-21389-8
576   (2018).

577 25 Focosi, D., Bestagno, M., Burrone, O. & Petrini, M. CD57+ T lymphocytes and
578   functional immune deficiency. *J Leukoc Biol* **87**, 107-116, doi:10.1189/jlb.0809566
579   (2010).
580 26 Mahnke, Y. D., Brodie, T. M., Sallusto, F., Roederer, M. & Lugli, E. The who's who
581   of T-cell differentiation: Human memory T-cell subsets. *European Journal of*
582   *Immunology* **43**, 2797-2809, doi:doi:10.1002/eji.201343751 (2013).
583 27 Xin, G. *et al.* Single-cell RNA sequencing unveils an IL-10-producing helper subset
584   that sustains humoral immunity during persistent infection. *Nature*
585   *Communications* **9**, 5037, doi:10.1038/s41467-018-07492-4 (2018).
586 28 Piedra-Quintero, Z. L., Wilson, Z., Nava, P. & Guerau-de-Arellano, M. CD38: An
587   Immunomodulatory Molecule in Inflammation and Autoimmunity. *Frontiers in*
588   *Immunology* **11**, doi:10.3389/fimmu.2020.597959 (2020).
589 29 Jung, J. H. *et al.* SARS-CoV-2-specific T cell memory is sustained in COVID-19
590   convalescent patients for 10 months with successful development of stem cell-like
591   memory T cells. *Nature Communications* **12**, 1-12, doi:doi:10.1038/s41467-021-
592   24377-1 (2021).
593 30 De Biasi, S. *et al.* Marked T cell activation, senescence, exhaustion and skewing
594   towards TH17 in patients with COVID-19 pneumonia. *Nature Communications* **11**,
595   3434, doi:10.1038/s41467-020-17292-4 (2020).
596 31 Bouadma, L. *et al.* Immune Alterations in a Patient with SARS-CoV-2-Related
597   Acute Respiratory Distress Syndrome. *J Clin Immunol* **40**, 1082-1092,
598   doi:10.1007/s10875-020-00839-x (2020).
599 32 Im, S. J. *et al.* Defining CD8+ T cells that provide the proliferative burst after PD-1
600   therapy. *Nature* **537**, 417-421, doi:doi:10.1038/nature19330 (2016).
601 33 He, R. *et al.* Follicular CXCR5-expressing CD8+ T cells curtail chronic viral
602   infection. *Nature* **537**, 412-416, doi:10.1038/nature19317 (2016).
603 34 Leong, Y. A. *et al.* CXCR5+ follicular cytotoxic T cells control viral infection in B
604   cell follicles. *Nature Immunology* **17**, 1187-1196, doi:doi:10.1038/ni.3543 (2016).
605 35 Yu, D. & Ye, L. A Portrait of CXCR5+ Follicular Cytotoxic CD8+ T cells. *Trends in*
606   *Immunology* **39**, 965-979, doi:10.1016/j.it.2018.10.002 (2018).
607 36 Quigley, M. F., Gonzalez, V. D., Granath, A., Andersson, J. & Sandberg, J. K.
608   CXCR5+ CCR7- CD8 T cells are early effector memory cells that infiltrate tonsil B
609   cell follicles. *Eur J Immunol* **37**, 3352-3362, doi:10.1002/eji.200636746 (2007).
610 37 Wu, T. *et al.* The TCF1-Bcl6 axis counteracts type I interferon to repress
611   exhaustion and maintain T cell stemness. *Sci Immunol* **1**,
612   doi:10.1126/sciimmunol.aai8593 (2016).
613 38 Kalish, H. *et al.* Undiagnosed SARS-CoV-2 seropositivity during the first 6 months
614   of the COVID-19 pandemic in the United States. *Science Translational Medicine*
615   **13**, eabh3826, doi:doi:10.1126/scitranslmed.abh3826 (2021).
616 39 Jones, J. M. *et al.* Estimated US Infection- and Vaccine-Induced SARS-CoV-2
617   Seroprevalence Based on Blood Donations, July 2020-May 2021. *JAMA* **326**,
618   1400-1409, doi:10.1001/jama.2021.15161 (2021).
619 40 Files, J. K. *et al.* Sustained cellular immune dysregulation in individuals recovering
620   from SARS-CoV-2 infection. *The Journal of Clinical Investigation* **131**,
621   doi:10.1172/JCI140491 (2021).

622   41   Gaebler, C. *et al.* Evolution of antibody immunity to SARS-CoV-2. *Nature* **591**,
623   639-644, doi:10.1038/s41586-021-03207-w (2021).
624   42   Breton, G. *et al.* Persistent cellular immunity to SARS-CoV-2 infection. *Journal of*
625   *Experimental Medicine* **218**, doi:10.1084/jem.20202515 (2021).
626   43   Roukens, A. H. E. *et al.* Prolonged activation of nasal immune cell populations and
627   development of tissue-resident SARS-CoV-2-specific CD8+ T cell responses
628   following COVID-19. *Nature Immunology* **23**, 23-32, doi:10.1038/s41590-021-
629   01095-w (2022).
630   44   Szabo, P. A., Miron, M. & Farber, D. L. Location, location, location: Tissue resident
631   memory T cells in mice and humans. *Science immunology* **4**, eaas9673,
632   doi:10.1126/sciimmunol.aas9673 (2019).
633   45   Yoshida, M. *et al.* Local and systemic responses to SARS-CoV-2 infection in
634   children and adults. *Nature* **602**, 321-327, doi:10.1038/s41586-021-04345-x
635   (2022).
636   46   Pierce, C. A. *et al.* Natural mucosal barriers and COVID-19 in children. *JCI Insight*
637   **6**, doi:10.1172/jci.insight.148694 (2021).
638   47   Daniel, C. *et al. Nature Portfolio*, doi:10.21203/rs.3.rs-1139035/v1 (2022).
639   48   Bergqvist, P. *et al.* Re-utilization of germinal centers in multiple Peyer's patches
640   results in highly synchronized, oligoclonal, and affinity-matured gut IgA responses.
641   *Mucosal Immunol* **6**, 122-135, doi:10.1038/mi.2012.56 (2013).
642   49   Meng, W. *et al.* An atlas of B-cell clonal distribution in the human body. *Nature*
643   *Biotechnology* **35**, 879-884, doi:10.1038/nbt.3942 (2017).
644   50   Ohm-Laursen, L. *et al.* B Cell Mobilization, Dissemination, Fine Tuning of Local
645   Antigen Specificity and Isotype Selection in Asthma. *Frontiers in Immunology* **12**,
646   doi:10.3389/fimmu.2021.702074 (2021).
647   51   Schwickert, T. A., Alabyev, B., Manser, T. & Nussenzweig, M. C. Germinal center
648   reutilization by newly activated B cells. *Journal of Experimental Medicine* **206**,
649   2907-2914, doi:10.1084/jem.20091225 (2009).
650   52   Schwickert, T. A. *et al.* In vivo imaging of germinal centres reveals a dynamic open
651   structure. *Nature* **446**, 83-87, doi:10.1038/nature05573 (2007).
652   53   Hoehn, K. B. *et al.* Human B cell lineages associated with germinal centers
653   following influenza vaccination are measurably evolving. *Elife* **10**,
654   doi:10.7554/eLife.70873 (2021).
655   54   Carrasco, A. *et al.* The Tonsil Lymphocyte Landscape in Pediatric Tonsil
656   Hyperplasia and Obstructive Sleep Apnea. *Frontiers in Immunology* **12**,
657   doi:10.3389/fimmu.2021.674080 (2021).
658   55   Feldstein, L. R. *et al.* Characteristics and Outcomes of US Children and
659   Adolescents With Multisystem Inflammatory Syndrome in Children (MIS-C)
660   Compared With Severe Acute COVID-19. *JAMA* **325**, 1074-1087,
661   doi:10.1001/jama.2021.2091 (2021).
662   56   Vella, L. A. *et al.* Deep immune profiling of MIS-C demonstrates marked but
663   transient immune activation compared to adult and pediatric COVID-19. *Science*
664   *Immunology* **6**, eabf7570, doi:10.1126/sciimmunol.abf7570 (2021).
665   57   Sacco, K. *et al.* Immunopathological signatures in multisystem inflammatory
666   syndrome in children and pediatric COVID-19. *Nature Medicine*,
667   doi:10.1038/s41591-022-01724-3 (2022).

668   **Figure 1**
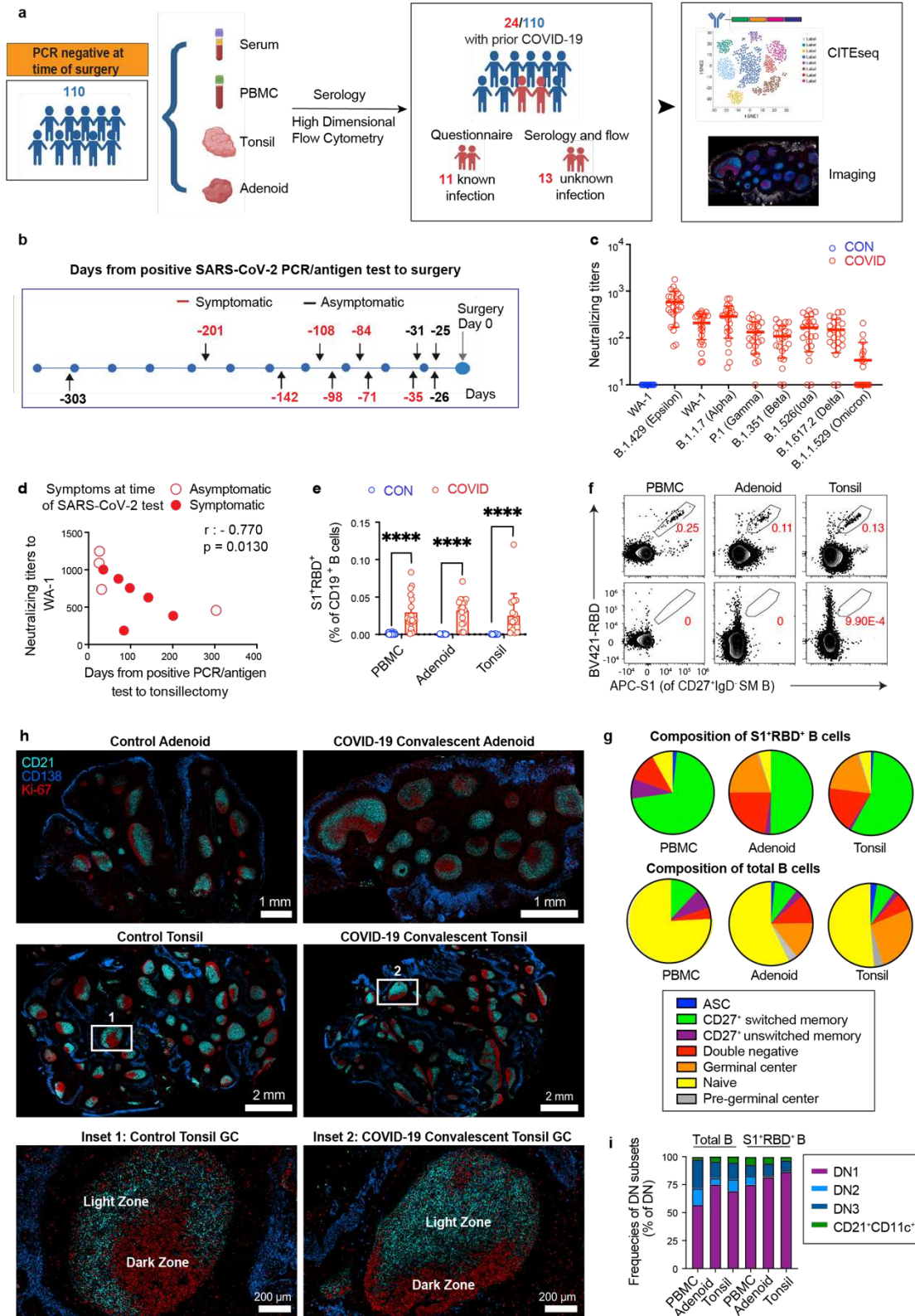
669
670   **Figure 1. SARS-CoV-2 elicits robust humoral immune responses in children**

a. Participant enrollment and study design.

b. Time from positive SARS-CoV-2 PCR/antigen test from nasopharyngeal swab to tonsillectomy and/or adenoidectomy surgery.

c. Neutralization titers (PsVNA50) against the early isolate WA-1 and seven other SARS-CoV-2 variants of interest in COVID-19 convalescent subjects (COVID) vs. controls (CON) (COVID n=23, CON n=14, samples listed in Supplementary Table 4).

d. Correlation between neutralizing antibody titers to WA-1 and days from positive SARS-CoV-2 test to surgery (n = 10).

e. Frequency of $S1^+RBD^+$ cells among total $CD19^+$ B cells from PBMC, adenoid, and tonsil from COVID vs. CON (PBMC COVID n = 18, CON n = 33; adenoid COVID n = 16, CON n = 27; and tonsil COVID n = 16, CON n = 30).

f. Representative flow cytometry plots demonstrating the percentage of SARS-CoV-2-specific ($S1^+RBD^+$) cells among $CD27^+IgD^-$ switched memory B cells in PBMC, adenoid, and tonsil following COVID-19. Gating strategy shown in Supplementary Fig 1-2.

g. Composition of $S1^+RBD^+$ B cells and total B cells from PBMC, adenoid, and tonsil from COVID-19 convalescent subjects. Mean frequency of each B cell subset is presented in the pie chart. B cell subsets are defined in Supplementary Fig 1-2. ASC = antibody secreting cells, equivalent to plasma cells and plasmablasts.

h. Representative images of adenoid and tonsil from a COVID-19-convalescent donor showing multiple, intact germinal centers (GCs) comparable to that from controls. Inset shows close-up of GC with discrete light and dark zones. CD21 (follicular dendritic cells, light zone) in cyan, Ki-67 (dividing cells, dark zone) in red, CD138 (plasma cells and epithelial cell marker) in blue.

i. Composition of $S1^+RBD^+$ double negative (DN) B cells and total DN B cells from PBMC, adenoid, and tonsil (COVID PBMC n = 18, adenoid n = 16, tonsil n = 16). Mean frequency of each DN subset is presented in the bar chart.

Each symbol represents data from one donor. Means ± S.D. are displayed in the scatter and bar plots. Significance calculated with Mann-Whitney U test. Correlations assessed with Spearman's rank correlation. **** p<0.0001.
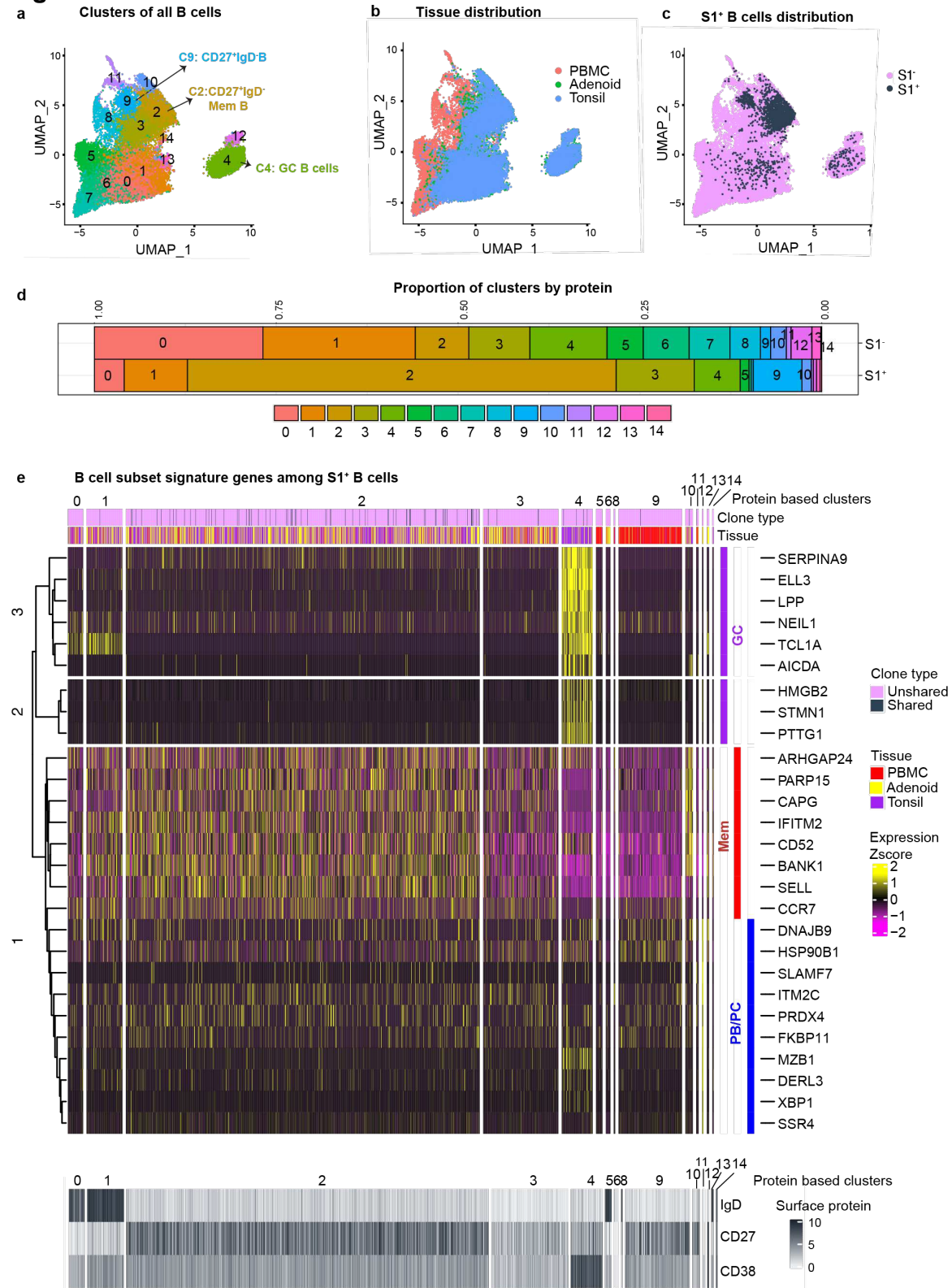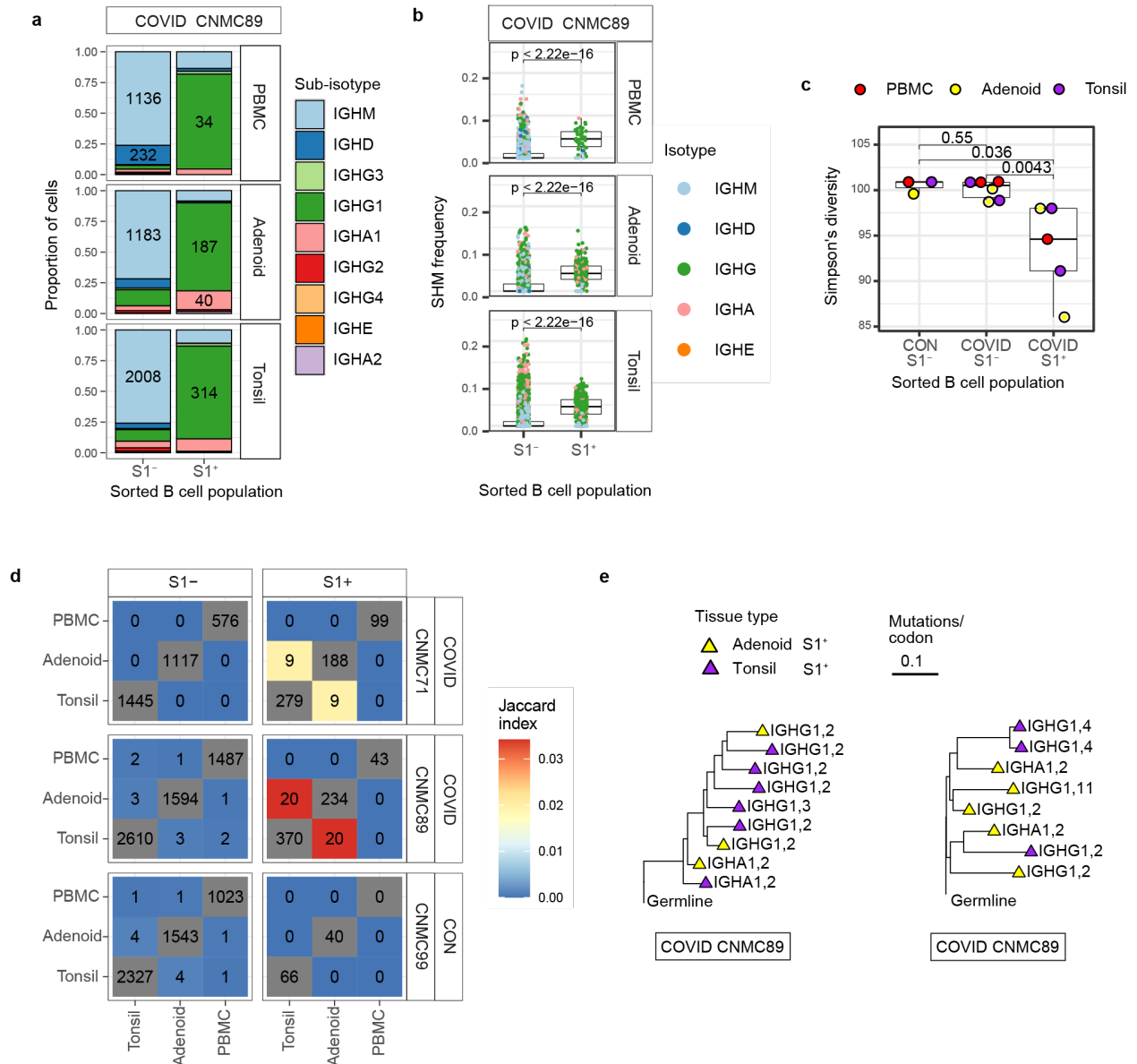
Figure 2

Figure 2. CITE-seq analysis of SARS-CoV-2 antigen-specific B cells

703   a. Uniform manifold approximation and projection (UMAP) showing 15 clusters of sorted

704   S1$^+$ and S1$^-$ B cells from tonsil, adenoid, and PBMCs of three donors (2 COVID-19-

705   convalescent and 1 control) clustered according to CITE-seq surface antibody expression.

706   b and c. Tissue distribution of cells is shown in b. S1$^+$ B cells are highlighted c.

707   d. Proportion of each cluster among S1$^-$ and S1$^+$ B cells.

708   e. Heat map showing expression of signature gene sets for germinal center B cells (GC),

709   memory B cells(Mem), and plasma cells/plasmablasts (PB/PC)[18] among S1$^+$ B cells

710   organized by cluster. IgD, CD38, and CD27 CITE-seq antibody expression are shown in

711   lower heat map in grey. Tissue origin is shown in purple (tonsil), yellow (adenoid), and red

712   (PBMC), while clones shared between tonsil and adenoid are marked in black in the top

713   bar. Sorting strategy shown in Supplementary Fig. 3.

Figure 3

717 **Figure 3. Single cell BCR sequencing of SARS-CoV-2 antigen-specific B cells**

718 a. Sub-isotype frequencies among S1$^+$ and S1$^-$ B cells from PBMC, adenoid, and tonsil of

719 one COVID-19 convalescent donor (CNMC 89). Labels show the raw number of cells with

720 a given sub-isotype and are only included for sub-isotypes that make up at least 10% of a

721 given category.

722 b. Somatic hypermutation (SHM) frequency among S1$^+$ and S1$^-$ B cells from PBMC,

723 adenoid, and tonsil of CNMC 89. Mutation frequency calculated in V gene.

724   c. Simpson's diversity of S1$^+$ and S1$^-$ B cells from PBMCs, adenoids, and tonsils from 2

725   COVID-19 convalescent donors (COVID, CNMC 71 and 89) and one control (CON, CNMC

726   99). Lower Simpson's diversity values indicate a greater frequency of large clones. To

727   adjust for sequence depth, diversity is calculated as the mean of 1000 uniform resampling

728   repetitions.

729   d. Overlap of B cell clones among PBMC, tonsil, and adenoid from COVID and CON. Off-

730   diagonal elements are colored by the Jaccard index of clonal overlap between the two

731   tissues and are labelled by the raw number of overlapping clones. Diagonal elements are

732   labelled by the total number of clones within a particular tissue.

733   e. Clonal lineage trees from two of the largest S1$^+$ B cell clones shared between tonsil and

734   adenoid from CNMC 89. Triangles indicate S1$^+$ cells, and tip color indicates tissue of origin.

735   Isotype and CITE-seq cluster of each cell are listed next to the symbol. Branch lengths

736   represent SHM frequency/codon in VDJ sequence according to the scale bar.

737   Significance calculated with Mann Whitney U test.

738

Figure 4

740
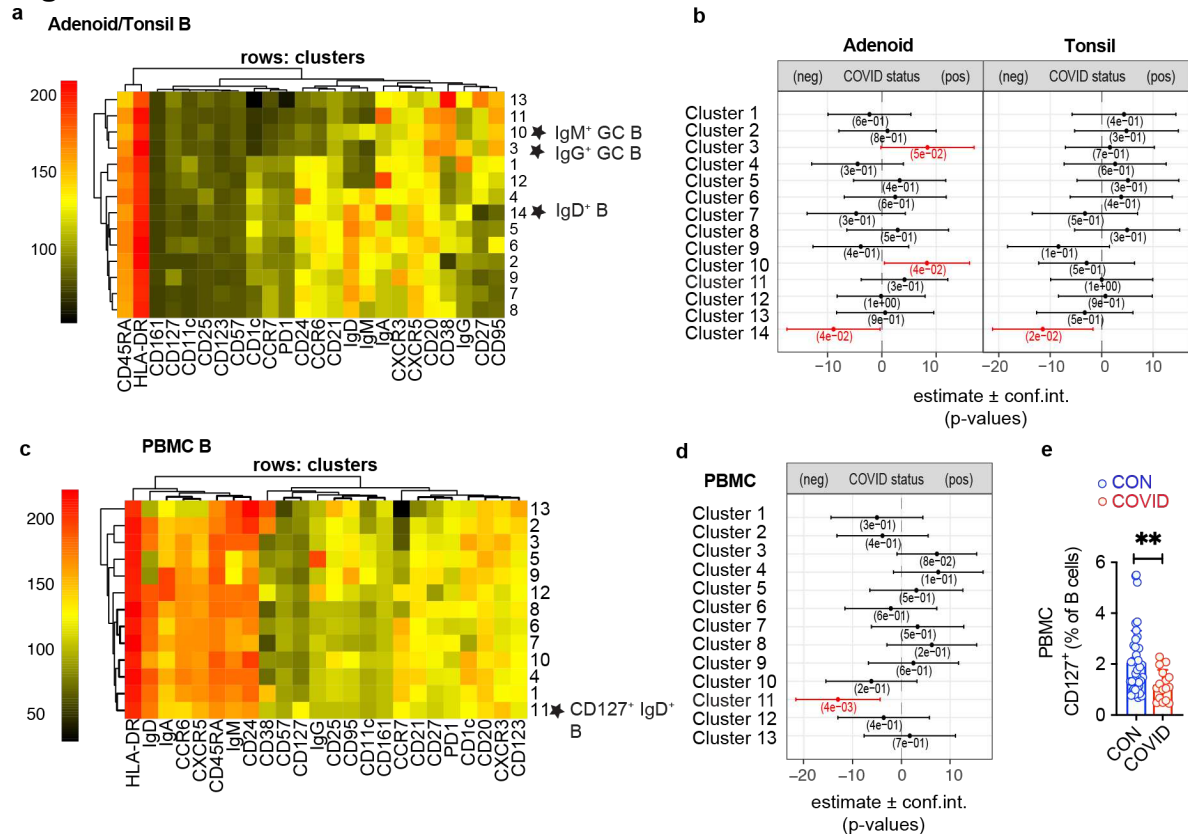
Figure 4. GC B cells are expanded in adenoids after COVID-19

a and c. Unsupervised clustering of CD19$^+$ B cells from adenoid and tonsil (a) and PBMC (c) according to flow cytometric surface markers. Stars indicate clusters with significant differences (p<0.05) in COVID-19-convalescent samples (COVID) vs. controls (CON) (COVID adenoid n = 11, CON adenoid n = 33, COVID tonsil n = 15, CON tonsil n = 42, COVID PBMC n = 14, CON PBMC n = 36).
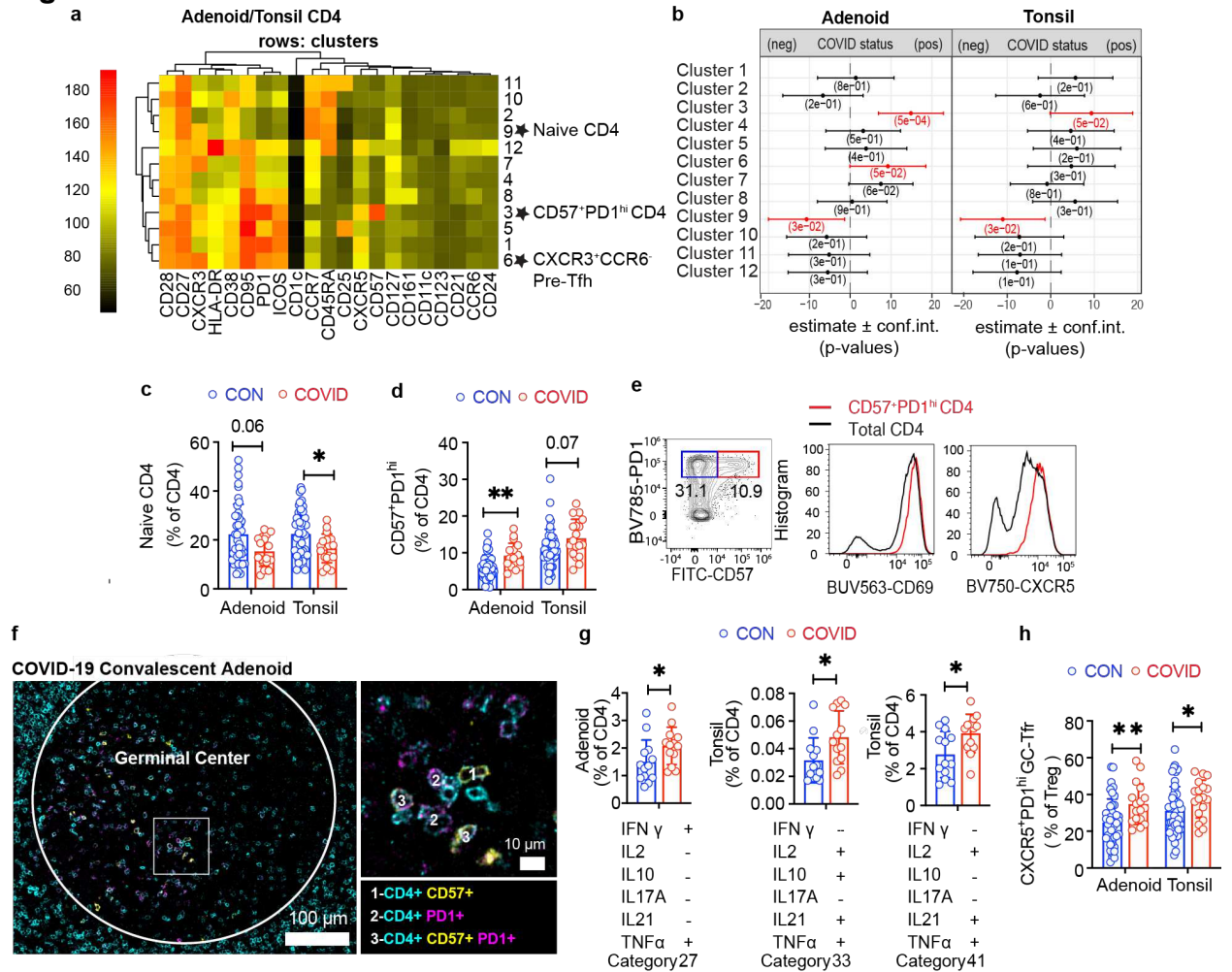
b and d. Quantification of the effect of prior SARS-CoV-2 infection on CD19$^+$ B cell clusters in adenoid and tonsil (b) and PBMC (d) estimated with a linear model controlling for age and sex. Regression coefficients with 95% confidence intervals and p values are shown. Significantly different clusters are highlighted in red. Analyzed samples are listed in Supplementary Table 2. Statistical analysis described in Methods.

e. Frequency of CD127$^+$ B cells in PBMC of COVID (n = 16) vs. CON (n = 41). Significance calculated using Mann-Whitney U test. Each symbol represents data from one donor. Mean ± S.D. are displayed. ** p<0.01.

Figure 5

Figure 5. CD4+ Tfh cells are expanded in pharyngeal tissues post-COVID-19

a. Unsupervised clustering of CD4+ T cells from adenoid and tonsil according to surface

markers from flow cytometry. Stars indicate clusters with significant differences (p<0.05)

in COVID-19-convalescent samples (COVID) vs. controls (CON) (COVID adenoid n = 12,

CON adenoid n = 38, COVID tonsil n = 15, CON tonsil n = 43).

b. Quantification of the effect of prior SARS-CoV-2 infection on CD4+ T cell clusters in

adenoid and tonsil estimated with a linear model controlling for age and sex. Regression

coefficients with 95% confidence intervals and p values are shown. Significantly different

clusters are highlighted in red. Statistical analysis is described in Methods.

c. and d. Frequencies of naïve (CD45RA+CCR7+) CD4+ T cells (c) and CD57+PD-1hi CD4+

T cells (d) in adenoids and tonsils of COVID vs. CON.

e. Representative plots of CD69 and CXCR5 expression on CD57$^+$PD-1^{hi} CD4$^+$ T cells vs. total CD4$^+$ T cells from tonsil. Phenotypes are similar in adenoid.

f. Representative multicolor immunofluorescence staining of COVID adenoid showing the location of CD57$^+$PD-1^{hi} CD4$^+$ T cells in the GC. CD4 shown in cyan, CD57 in yellow, and PD-1 in magenta. GC boundaries were defined using Ki-67 (not shown) as demonstrated in Figure 1h.

g. Significantly different cytokine combinations produced by tonsillar and adenoid CD4$^+$ T cells from COVID (n = 13) vs. CON (n = 13) following PMA and ionomycin stimulation. Fifty-nine combinations of cytokines (IFN-γ, IL-2, IL-10, IL-17A, IL-21, and TNF-α) made by CD4$^+$ T cells were included in the SPICE analysis (see Supplementary Fig. 6).

h. Frequencies of CXCR5$^+$PD-1^{hi} GC-Tfr cells in adenoid and tonsil of COVID vs. CON. Gating strategy shown in Supplementary Figure 5. Samples analyzed in panels c-d and h are listed in Supplementary Table 2 (COVID adenoid n = 17, CON adenoid n = 42, COVID tonsil n = 18, CON tonsil n = 46). Samples included in panel f-g are listed in Supplementary Table 9. Each symbol represents data from one donor. Means ± S.D. are displayed on scatter and bar plots. Significance calculated using Mann-Whitney U test. * p<0.05, ** p<0.01.
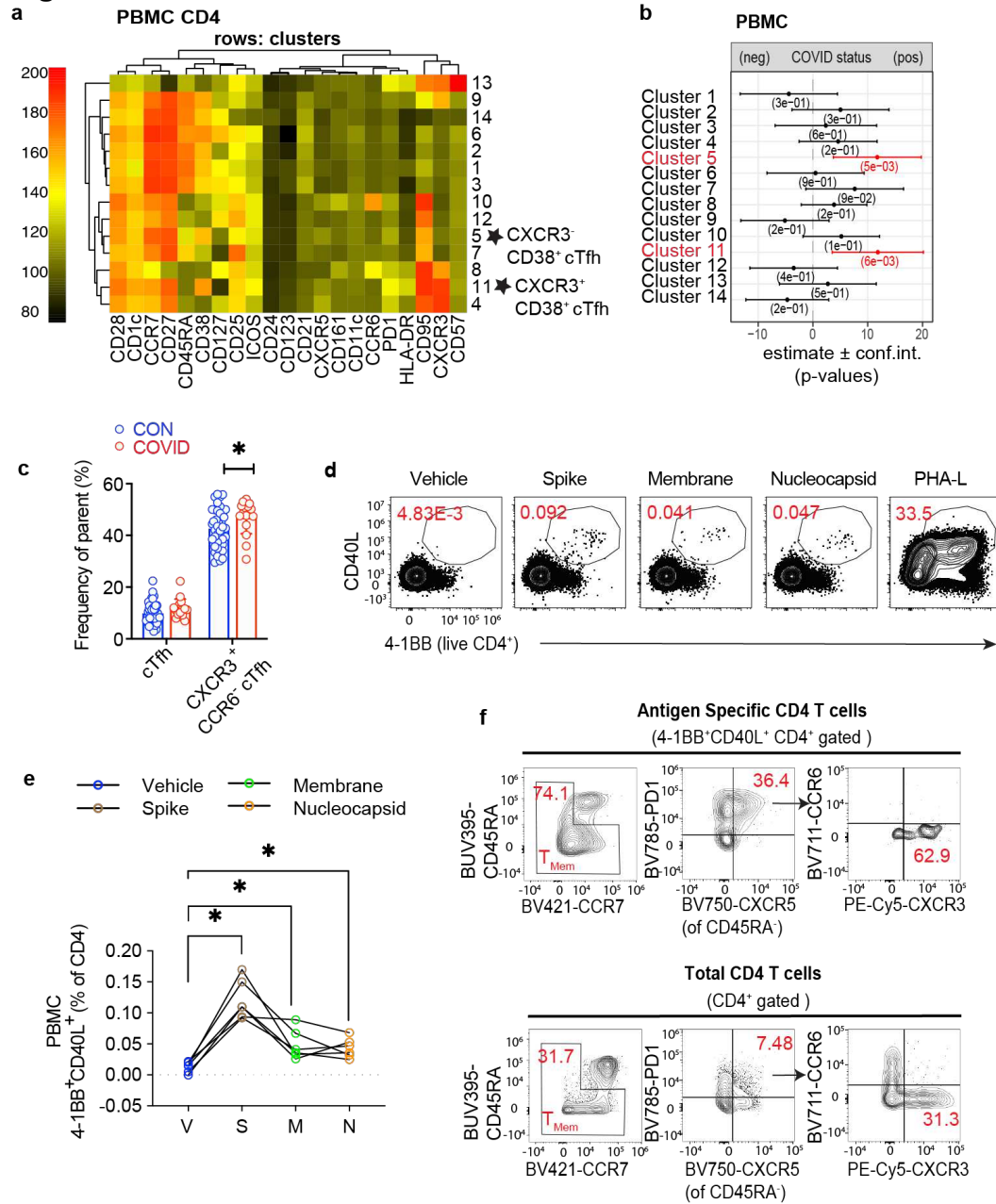
Figure 6

Figure 6. SARS-CoV-2 antigen-specific CD4^{+} T cells in PBMC following COVID-19

a. Unsupervised clustering of CD4^{+} T cells from PBMC according to surface markers

from flow cytometric analysis. Stars indicate clusters with significant differences (p<0.05)

in COVID-19-convalescent samples (COVID) vs. controls (CON) (COVID n = 13, CON n

= 34).

b. Quantification of the effect of prior SARS-CoV-2 infection on CD4^{+} T cell clusters in

PBMC estimated with a linear model controlling for age and sex. Regression coefficients

795 with 95% confidence intervals and p values are shown. Significantly different clusters are

796 highlighted in red. Statistical analysis is described in Methods.

797 c. Frequencies of cTfh (CD45RA$^-$CXCR5$^+$PD-1$^+$) and CXCR3$^+$CCR6$^-$ cTfh cells in PBMC

798 of COVID (n=16) vs. CON (n=41). Significance calculated with Mann-Whitney U.

799 d. Representative flow cytometry plots showing gating of antigen-specific CD4$^+$ T cells

800 from PBMC of a COVID-19-convalescent donor expressing activation induced markers

801 (AIM$^+$: CD40L$^+$4-1BB$^+$) following stimulation with SARS-CoV-2 peptide pools of spike,

802 membrane, and nucleocapsid. DMSO was used as negative control (vehicle), and PHA-L

803 was used as positive control.

804 e. Frequencies of AIM$^+$ CD4$^+$ T cells from PBMC of COVID-19-convalescent donors

805 following SARS-CoV-2 peptide pool stimulation (n = 6). Significance calculated with

806 Wilcoxon signed rank test for paired samples from the same donor.

807 f. Flow cytometry plots showing frequency of T$_{Mem}$, cTfh (CD45RA$^-$CXCR5$^+$PD-1$^+$), and

808 CXCR3$^+$CCR6$^-$ cTfh cells from concatenated antigen-specific CD4$^+$ T cells following

809 SARS-CoV-2 peptide stimulation compared to total CD4$^+$ T cells in PBMC. AIM$^+$ CD4$^+$ T

810 cells were concatenated from all three peptide pool stimulations from all 6 donors.

811 Gating strategy shown in Supplementary Figure 8. Samples used in AIM analyses are

812 shown in Supplementary Table 9. * p<0.05.
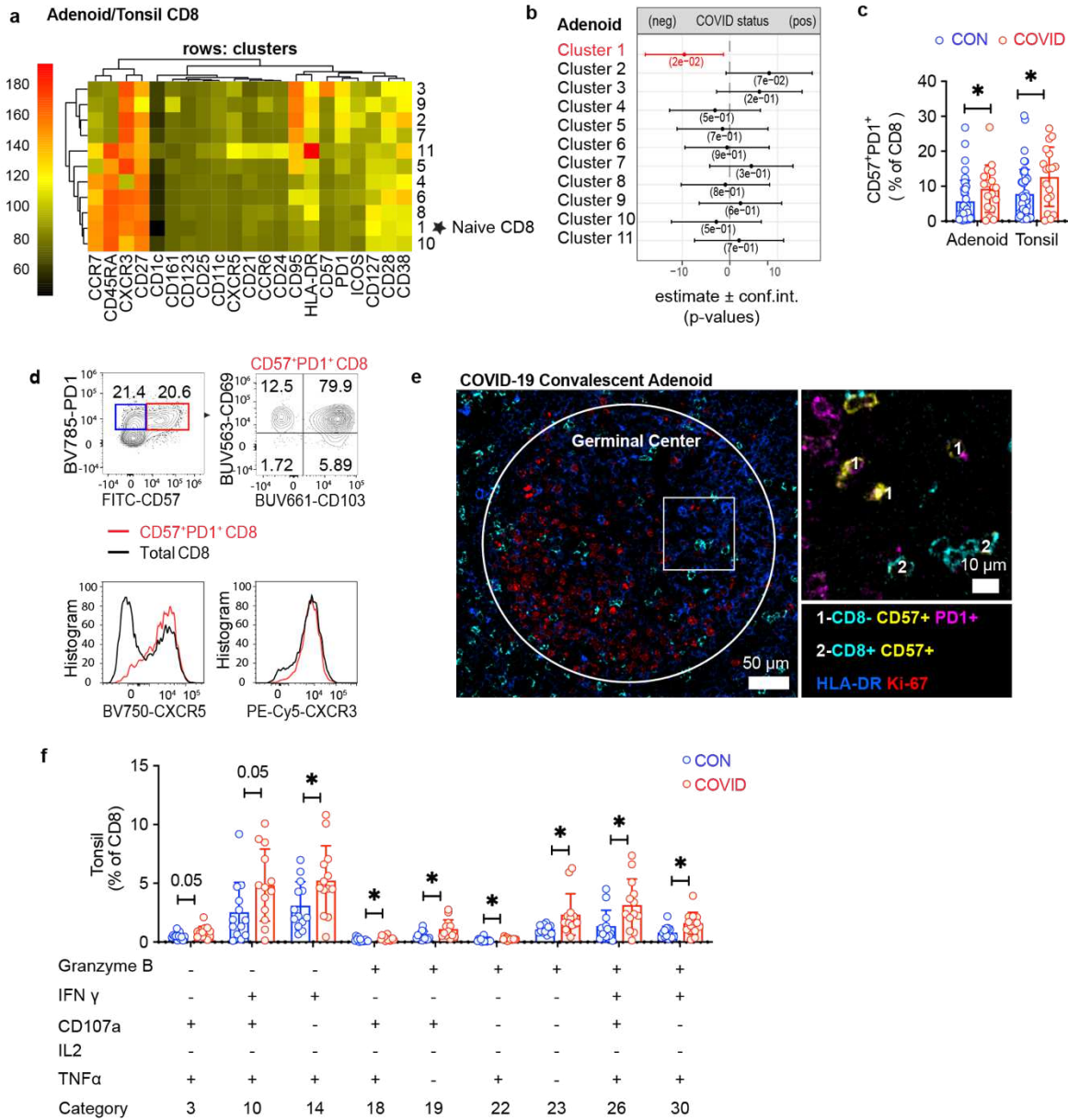
Figure 7

815 **Figure 7. Tissue-resident memory CD8+ T cells are expanded in pharyngeal tissues**

816 **post-COVID-19**

817 a. Unsupervised clustering of CD8+ T cells from adenoid and tonsil according to surface

818 antibody expression from flow cytometry analysis. Stars indicate clusters with significant

819 differences (p<0.05) in COVID-19-convalescent samples (COVID) vs. controls (CON).

820 (COVID adenoid n = 12, CON adenoid n = 35, COVID tonsil n = 15, CON tonsil n = 42).

821   b. Quantification of the effect of prior SARS-CoV-2 infection on CD8$^+$ T cell clusters in

822   adenoid estimated with a linear model controlling for age and sex. Regression

823   coefficients with 95% confidence intervals and p values are shown. Significantly different

824   clusters are highlighted in red. Statistical analysis is described in Methods.

825   c. Frequency of CD57$^+$PD-1$^+$ CD8$^+$ T cells in adenoid and tonsil from COVID vs. CON

826   (COVID adenoid n = 17, CON adenoid n = 42, COVID tonsil n = 18, CON tonsil n = 46).

827   d. Representative flow cytometry plots showing CD69, CD103, CXCR5, and CXCR3

828   expression on CD57$^+$PD-1$^+$ CD8$^+$ T cells from tonsil. Phenotypes are similar in adenoid.

829   e. Representative multicolor immunofluorescence staining of adenoid from COVID-19-

830   convalescent donor showing the location of CD57$^+$PD-1$^+$ CD8$^+$ T in the GC. CD8 is

831   shown in cyan, CD57 is yellow, PD-1 is pink. HLA-DR (blue) stains follicles, and Ki-67

832   (red) stains GC.

833   f. Significantly different cytokine combinations produced by tonsillar CD8$^+$ T cells from

834   COVID (n=13) vs. CON (n=13) following PMA and ionomycin stimulation. Thirty-one

835   combinations of cytotoxic factors and cytokines (granzyme B, IFN-γ, CD107a, IL-2 and

836   TNF-α) made by CD8$^+$ T cells were included in the SPICE analysis (see Supplementary

837   Fig. 9).

838   Gating strategy shown in Supplementary Figure 5. Samples analyzed in panels a-c are

839   listed in Supplementary Table 2. Samples included in panels e-f are listed in

840   Supplementary Table 9. Each symbol represents data from one donor. Means ± S.D. are

841   displayed in scatter and bar plots. Significance calculated using Mann-Whitney U test. *

842   p<0.05.

843   **Figure 8**
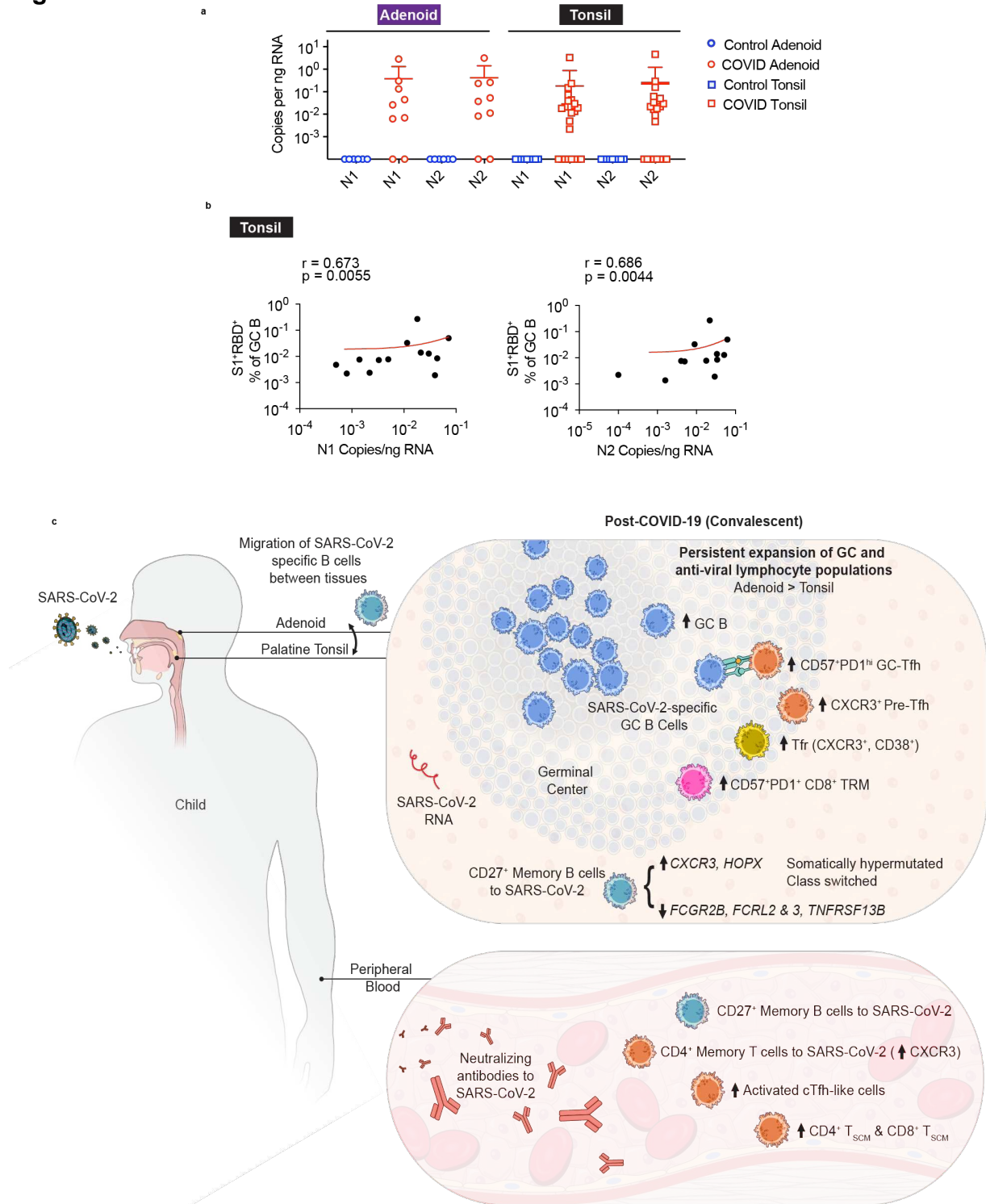
844
845   **Figure 8. Persistence of SARS-CoV-2 RNA in the pharyngeal tissues post-COVID-19**

846   a. Quantification of SARS-CoV-2 nucleocapsid RNA by digital droplet PCR (ddPCR) from

847   adenoid and tonsil FFPE tissue blocks (COVID adenoid n = 9, control adenoid = 6, COVID

848   tonsil n = 22, control tonsil n = 9). N1 and N2 represent two regions of the gene encoding

849   the SARS-CoV-2 nucleocapsid. Each symbol represents data from one donor. Means ±

850   S.D. are displayed.

851   b. Correlation of nucleocapsid (N1 and N2) copies per nanogram RNA with percentage of

852    $S1^+RBD^+$ B cells among GC B cells from tonsils following SARS-CoV-2 infection (COVID

853   tonsil n = 13).

854   c. Schematic illustrating the immunologic profile of the oropharyngeal lymphoid tissues and

855   peripheral blood of COVID-19-convalescent children including (1) SARS-CoV-2-specific

856   GC and memory B cells with overlapping clones in the tonsils and adenoids, (2) persistent

857   changes in lymphocyte populations involved in germinal center and anti-viral responses,

858   which were most prominent in the adenoid, with type 1 skewing of several T lymphocyte

859   populations, and (3) persistence of viral RNA in the tissue.

860   Samples analyzed are in Supplementary Table 7. Each symbol represents data from one

861   donor. Means ± S.D. are displayed in scatter plots. Correlations assessed with Spearman's

862   rank correlation.

Methods

Ethics statement

This study was approved by the Institutional Review Board (IRB) at Children's National Hospital (IRB protocol number 00009806). Written informed consent was obtained from parent/guardians of all enrolled participants, and assent was obtained from minor participants over 7 years of age.

Participant recruitment

We recruited 110 children who underwent tonsillectomy and/or adenoidectomy at Children's National Hospital (CNH) in Washington, DC, USA. All children scheduled to undergo tonsillectomy at CNH were eligible. The first 102 participants were recruited from late September 2020 to early February 2021 without screening for prior COVID-19. An additional 2 participants were subsequently recruited with known history of COVID-19, plus 6 additional subjects (one of whom turned out to be positive by serology) were recruited in May and June 2021. Because not all tissues or blood were available from each subject, we collected a total of 106 blood samples, 100 adenoids, and 108 tonsils from 110 participants (Supplementary Table 2). No statistical methods were used to predetermine sample size. All participants had negative RT-PCR testing from a nasopharyngeal swab for SARS-CoV-2 within 72 hours of the surgery. Demographic information and clinical data were collected through parental questionnaires and chart review and inputted and managed in REDCap, and biologic samples were acquired in the operating room by a separate clinical team at CNH.

Eleven participants had previous confirmed SARS-CoV-2 infection with RT-PCR or antigen testing from nasopharyngeal swabs. Another thirteen COVID-19-exposed participants were identified through serum antibody testing and/or identification of B cells that recognize the spike protein of SARS-CoV-2 by flow cytometry (described below). One participant (CNMC 43) had SARS-CoV-2 detected by RT-PCR from the nasopharynx 20 days prior to surgery but had negative serology and no SARS-CoV-2 specific B cells in the tissue or blood. We excluded this subject from our subsequent analysis.

Control selection within the cohort

Controls for flow cytometric analyses were selected among subjects with no serologic or cellular evidence of prior COVID-19. The primary indication for tonsillectomy in all 24 participants with prior COVID-19 was adenotonsillar hypertrophy leading to sleep disordered breathing (SDB) or obstructive sleep apnea (OSA) (Supplementary Table 1 and 3) except one participant who had eustachian tube dysfunction. Patients with SDB and OSA both have breathing difficulties during sleep (primarily snoring); however, patients with OSA had polysomnography documenting an apnea-hypopnea index greater than 1, while those with SDB did not undergo polysomnography testing and were diagnosed by clinical history alone. None of the 24 participants with COVID-19 had frequent recurrent tonsillitis (more than 6 episodes in a year) or other medical problems that directly affect the immune system aside from atopic disease, nor did they take immunomodulating medications aside from nasal/inhaled steroid or loratadine within 2 weeks of surgery. Therefore, subjects were excluded from the control group if they (a) had periodic fever, recurrent tonsillitis or chronic tonsillitis as primary indication for surgery (N = 15); (b) had more than 6 episodes of tonsillitis in a year (N = 2); (c) took immunomodulatory medications (including montelukast and cetirizine) aside from inhaled steroid or loratadine within 2 weeks of surgery (N = 9); (d) had sickle cell anemia (N = 3), or (e) did not have flow cytometry studies performed on their samples on the day of processing due to sample collection prior to panel finalization or technical problems with the flow cytometer on the day of acquisition. Controls were also excluded if they had indeterminate serologic testing for SARS-CoV-2 infection and did not have any SARS-CoV-2 specific B cells in the tissue or blood (N = 2); both of these participants subsequently had negative neutralizing titers to SARS-CoV-2 as well. Samples included in unsupervised and manual gating analyses of flow cytometry data are listed in Supplementary Table 2.

Blood and tissue collection

Blood samples were obtained just prior to the surgical procedure in the operating room in serum separator tubes (BD) for serum collection and sodium heparin tubes (BD) for peripheral blood mononuclear cells (PBMCs) extraction from an intravenous line placed for

920   anesthesia. Once received in the laboratory on the day of collection, serum separator tubes
921   were spun at 1200g for 10 min, and serum was aliquoted and stored at -80°C. PBMCs
922   were isolated the day after collection by density gradient centrifugation (Lymphocyte
923   Separation Medium, MP Biomedicals) at 1500rpm for 30 min at room temperature with no
924   brake and washed with PBS. If red blood cell contamination was present, cells were lysed
925   with ACK buffer.

926   Tonsil and adenoid tissues were stored in RPMI media with 5% FBS (VWR), gentamicin
927   50mg/mL (Gibco), and 1X antibiotic/antimycotic solution (Gibco) on ice immediately after
928   collection. Tissues were processed the day after collection. A 3-5mm portion of tonsil and
929   adenoid tissue was cut and fixed in 5mL of 10% buffered formalin (Avantik) for 24-48 h.
930   The fixed tissue was then incubated in 70% ethanol until it was paraffin-embedded. The
931   remainder of the tissue was mechanically disrupted and filtered through a 100μm cell
932   strainer to create a single cell suspension, lysed with ACK buffer (Gibco), and washed with
933   PBS three times. Freshly isolated PBMCs and tonsil and adenoid cells were surface
934   stained and analyzed with flow cytometry as described below on the day of processing.
935   The remaining cells were stored in liquid nitrogen in the presence of FBS (VWR) with 10%
936   DMSO.

937   **SARS-CoV-2 serum antibody ELISA**

938   After thawing frozen serum to room temperature, IgG and IgM antibodies against the spike
939   (S) protein and receptor-binding domain (RBD) of the S protein of SARS-CoV-2 were
940   analyzed using ELISA as previously described[38,58]. Positivity thresholds were based on
941   mean optical density (absorbance) plus 3 standard deviations. The final criterion of S+ and
942   RBD+ for any combination of positive IgG or IgM gave estimated sensitivity and specificity
943   of 100% based on prior studies of this assay. Data are shown in Supplementary Table 4.

944   **Pseudovirus neutralization assay**

945   Antibody preparations were evaluated by SARS-CoV-2 pseudovirus neutralization assay
946   (PsVNA) using WA-1, B.1.429 (epsilon), B.1.1.7 (alpha), P.1 (gamma), B.1.351 (beta),

947 B.1.526 (iota), B.1.617.2 (delta), and B.1.1.529 (omicron) strains. The PsVNA using the

948 293-ACE2-TMPRSS2 cell line was described previously[59-61].

949 Briefly, human codon-optimized cDNA encoding SARS-CoV-2 S glycoprotein of the WA-1,

950 B.1.429, B.1.1.7, P.1, B.1.351, B.1.526, B.1.617.2, and B.1.1.529 strains were synthesized

951 by GenScript and cloned into eukaryotic cell expression vector pcDNA 3.1 between

952 the BamHI and XhoI sites. Pseudovirions were produced by co-transfection Lenti‑X 293T

953 cells with psPAX2(gag/pol), pTrip-luc lentiviral vector and pcDNA 3.1 SARS-CoV-2-spike-

954 deltaC19, using Lipofectamine 3000. The supernatants were harvested at 48h post

955 transfection and filtered through 0.45µm membranes and titrated using 293T-ACE2-

956 TMPRSS2 cells (HEK 293T cells that express ACE2 and TMPRSS2 proteins).

957 For the neutralization assay, 50 µL of SARS-CoV-2 S pseudovirions were pre-incubated

958 with an equal volume of medium containing serum at varying dilutions at room temperature

959 (RT) for 1 h, then virus-antibody mixtures were added to 293T-ACE2-TMPRSS2 cells in a

960 96-well plate. The input virus with all SARS-CoV-2 strains used in the current study were

961 the same ($2x10^5$ Relative light units/50 µL/well). After a 3 h incubation, the inoculum was

962 replaced with fresh medium. Cells were lysed 24 h later, and luciferase activity was

963 measured using luciferin. Controls included cells only, virus without any antibody and

964 positive sera. The cut-off value or the limit of detection for the neutralization assay is 1:10.

965 Data are shown in Supplementary Table 4.

966 **High-dimensional flow cytometry**

967 *SARS-CoV-2 antigen specific B cell detection*

968 5 million cells per sample of PBMC, adenoid, or tonsil were resuspended in PBS with 2%

969 FBS and 2 mM EDTA (FACS buffer). Biotinylated S1 and RBD probes (BioLegend) were

970 crosslinked with fluorochrome-conjugated streptavidin in a molar ratio of 4:1.

971 Fluorochrome-conjugated streptavidin was split into 5 aliquots and conjugated to

972 biotinylated S1 and RBD probes by mixing for 20 min/aliquot at 4°C. Cells were first stained

973 with the viability dye, Zombie NIR (1:800 dilution, BioLegend), for 15 min at RT, washed

974 twice and then incubated with True-Stain Monocyte Blocker (BioLegend) for 5 min. An

975 antibody cocktail containing the rest of the surface antibodies, the fluorochrome-

976   conjugated S1 and RBD probes, and Brilliant Stain Buffer Plus (BD) were then added
977   directly to the cells and incubated for 30 min at RT in the dark (200uL staining volume).
978   Cells were washed three times and fixed in 1% paraformaldehyde for 20 min at RT before
979   washing again and collecting on a spectral flow cytometer (Aurora, Cytek). Antibodies used
980   in this assay are shown in Supplementary Table 8.

981   ***Broad 37 parameter immunophenotyping flow cytometry panel***

982   2 million cells per sample of PBMC and 5 million cells per adenoid or tonsil were
983   resuspended in FACS buffer. Cells were first stained with LIVE/DEAD Blue (1:800,
984   ThermoFisher) for 15 min at RT, washed twice and then incubated with True-Stain
985   Monocyte Blocker (BioLegend) for 5 min. Antibodies for chemokine receptors and TCR$\gamma\delta$
986   were sequentially added at RT (anti-CCR7 for 10 min, anti-CCR6, anti-CXCR5 and anti-
987   CXCR3 together with Brilliant Stain Buffer Plus for 5 min, anti-TCR$\gamma\delta$ for 10 min). An
988   antibody cocktail containing the rest of the surface antibodies and Brilliant Stain Buffer Plus
989   were then added directly to the cells and incubated for 30 min at RT in the dark (total
990   staining volume 182uL). Cells were washed three times and stained with fluorescence
991   conjugated streptavidin for 15 min at RT. Then, cells were washed twice and fixed in 1%
992   paraformaldehyde for 20 min at RT before washing again and acquiring on the Aurora
993   spectral cytometer (Cytek). Antibodies used in this assay are shown in Supplementary
994   Table 8. The frequency of major populations was determined using FlowJo Software v10
995   (BD Biosciences) based on previously described manual gating strategies[62].

996   ***Unsupervised analysis of flow cytometry data and statistical modelling of meta-***
997   ***clustering results***

998   Data from the broad immunophenotyping flow cytometry panel with 37 parameters were
999   analyzed with unsupervised clustering of surface antibody staining. CD19$^+$ B cells, CD4$^+$ T
1000 cells, and CD8$^+$ T cells were analyzed separately. Tonsil and adenoid samples were
1001 merged and processed together while PBMC samples were processed separately due to
1002 pre-determined antibody concentration differences in staining required for optimal results
1003 in each organ. B cell analysis was based on surface expression of CCR6, CXCR5, CXCR3,
1004 CCR7, CD45RA, CD11c, IgD, CD20, IgM, IgG, CD27, HLA-DR, CD38, CD21, CD123, PD-

1005   1, CD57, CD25, CD24, CD95, IgA, CD1c, CD127 and CD161. CD4$^+$ and CD8$^+$ T cells

1006   analyses were based on the expression of CCR6, CXCR5, CXCR3, CCR7, CD45RA,

1007   CD161, CD28, PD-1, CD57, CD25, CD95, CD27, CD127, HLA-DR, CD38, ICOS, CD11c,

1008   CD24, CD1c, CD123, and CD21. FCS files (3.0) as well as FlowJo workspaces (10.7.2)

1009   were processed in R (4.1) via Rstudio (1.4.1717) and Bioconductor (3.13) using cytoverse

1010   (0.0.0.9000), including flowCore (2.4.0), flowWorkspace (4.4.0), ggcyto (1.20.0), openCyto

1011   (2.4.0), CytoML (2.4.0), cytolib (2.4.0) and cytoqc (0.99.2). Default options for biexponential

1012   data transformation were used. Outlier cells with expression values in the top or bottom

1013   1e-3 quantiles were excluded. Single cells in each sample were first clustered using k-

1014   means (k = 500, referred to as metacells), followed by merging cluster centroids from

1015   different samples with the same staining (i.e., tonsil/adenoids vs PBMC) for meta clustering

1016   and dimensionality reduction. Specifically, 500 centroids from each sample (metacells)

1017   were merged followed by another run of k-means meta-clustering (again k = 500), which

1018   were finally used in Leiden clustering and to learn a t-UMAP model to project the metacells

1019   (i.e., single cell-level k-means centroids; shown in plots). Seurat (4.0.3), uwot (0.1.10), and

1020   leiden (0.3.9) were used in shared nearest neighbors graph building, t-UMAP projection,

1021   and meta-clustering, respectively, with default settings. Leiden meta-clusters were mapped

1022   back to the single cell level and the ranked frequency of single cells in each Leiden meta-

1023   cluster in each sample was modeled linearly as a function of age, sex, and history of

1024   COVID-19 (COVID status) (as in lm(rank(frequency) ~ age + sex + status). Prior to

1025   statistical modeling, PCA of frequencies was used to detect and exclude outlier samples.

1026   Sample sizes are described in the legend of each plot. t-UMAP projections as well as all

1027   confidence intervals of coefficients and their p-values (from two-tailed t-test of each

1028   coefficient within each model) are presented in plots built with ggplot2 (3.3.5). Data are

1029   shown in Supplementary Table 10.

1030   **Single cell RNA sequencing**

1031   ***Processing for CITE-seq***

1032   Banked PBMC, tonsils and adenoids from 2 donors with history of COVID-19 (CNMC 71

1033   and 89) and one control (CNMC 99) were thawed from liquid nitrogen in a 37°C water bath

1034   for 2-3 mins. 2 mL of media consisting of RPMI with 10% of fetal bovine serum, 0.1mg/ml

1035   DNase I (Roche) and 10mM HEPES was added drop-by-drop to the thawed cells. Cells

1036   were further diluted by incremental addition of a 1:1 volume of media up to 8 mL, then

1037   centrifuged at 1600 rpm for 5 min. Cells were then resuspended in 300 µL of media,

1038   incubated at RT for 5 min, washed with media without DNase I, and filtered through a

1039   100µm strainer before spinning down for culture and resuspending in staining buffer (PBS

1040   + 1% BSA). Cells were then incubated with Fc blocker (Human TruStain FcX, BioLegend),

1041   stained with TotalSeq-C human hashtag antibodies (BioLegend) to uniquely label the

1042   sample origin (by tissue and donor), and washed with PBS + 0.04% BSA. Adenoids and

1043   tonsils from the 3 donors (6 samples in total) were pooled together and PBMCs from 3

1044   were pooled together separately. The number of cells to pool from each tissue and donor

1045   was calculated with the aim of pooling a similar number of $S1^+$ positive B cells from each

1046   sample. Pooled cells were first incubated with Fc blocker at 4°C for 10 min followed by

1047   CITE-seq and sorting antibody cocktails in the following order at 4°C: TotalSeq anti-CXCR3

1048   antibody for 10 min, TotalSeq chemokine cocktail (anti-CCR7, CCR6, CXCR5 antibodies)

1049   for 10 min, and the rest of CITE-seq antibodies and fluorescence-labeled sorting antibodies

1050   and viability dye (Aqua) for 30 min (Supplementary Table 8). Cells were then washed with

1051   PBS+0.04% BSA and resuspended in PBS+2% FBS. $S1^+$ and $S1^-$ B cells were sorted from

1052   each pool on a BD FACS Aria Fusion sorter for tonsil/adenoid pool and FACS Aria Illu

1053   sorter for the PBMC pool (BD Biosciences, San Jose, CA). See Supplementary Figure 3

1054   for sorting strategy. Cells were sorted into PBS+2% FBS. Note that the antibody

1055   concentrations used for CITE-seq were optimized by the manufacturer based on healthy

1056   PBMC samples, and thus may not be optimal for tissue samples. We have not

1057   independently verified the specificity of each antibody in our CITE-seq panel. Antibody

1058   concentrations were based on our titration from flow cytometry[63,64].

1059   Sorted $S1^+$ and $S1^-$ B cells were mixed with the reverse transcription mix and partitioned

1060   into single cell Gel-Bead in Emulsion (GEM) using 10x 5' Chromium Single Cell Immune

1061   Profiling Next GEM v2 chemistry (10x Genomics, Pleasanton, CA). The reverse

1062   transcription step was performed in an Applied Materials Veriti 96-well thermocycler. 10x

1063   Genomics 5' single cell gene expression, cell surface protein, and B cell receptor (BCR)

1064   libraries were prepared as instructed by 10x Genomics user guides

1065   (https://www.10xgenomics.com/resources/user-guides/). RNA quality and quantity in the

1066 libraries were measured using a bioanalyzer (Agilent, Santa Clara, CA) and a Qubit
1067 fluorometer (ThermoFisher). Libraires were pooled at a concentration of 10nM and
1068 sequenced on Illumina NovaSeq platform (Illumina, San Diego, CA) using the following
1069 read lengths: Read 1: 26 base pairs, Index 1: 10 base pairs, Index 2: 10 base pairs, Read
1070 2: 150 base pairs.

1071 ***CITE-seq data processing and analysis***

1072 CellRanger (10x Genomics) version 6.0.0 was used to map cDNA libraries to the hg19
1073 genome reference (10x genomics hg19 cellranger reference, version 1.2.0) and to count
1074 antibody tag features. Data were further processed using Seurat (v.4.0.1)[65] running in R
1075 v4.0.3. After transforming the surface protein library counts using *dsb*[66], we demultiplexed
1076 the pooled samples using manual cutoffs on the hashtag antibody staining. We removed
1077 cells with less than 100 detected genes, greater than 30% mitochondrial reads, or mRNA
1078 counts greater than 25,000. To exclude cells with extremely high surface antibody counts,
1079 we also removed the top 0.05% of cells in the surface antibody total count distribution. Cell
1080 clustering was performed by applying the FindNeighbors() function from *Seurat* on a
1081 distance matrix generated from the *dsb*-transformed surface protein data, followed by
1082 Louvain clustering on the resulting SNN graph using *Seurat's* FindClusters() algorithm, with
1083 a resolution parameter of 1. Expression of selected genes were visualized using the
1084 *ComplexHeatmap* package[67], and the percentage of cells per cluster for the $S1^+$ and $S1^-$
1085 cells was plotted using *ggplot2*[68]. For the comparison of differentially expressed genes
1086 between the $S1^+$ and $S1^-$ B cells, we first downsampled the fastq files from the $S1^+$
1087 sequencing library to more closely match the reads-per-cell obtained in the $S1^-$ sequencing
1088 libraries using *seqtk* v1.3. Differential expression was then compared using the MAST
1089 algorithm with "Donor" as a latent variable, as implemented in the Seurat *FindMarkers*
1090 function. For RNA-based clustering $S1^+$ and $S1^-$ B cells, we first downsampled the fastq
1091 files from the $S1^+$ sequencing library to more closely match the reads-per-cell obtained in
1092 the $S1^-$ sequencing libraries using *seqtk* v1.3. Cells were then clustered using the top 15
1093 PCs derived from the 2000 most variable genes, selected by Seurat's
1094 *FindVariableFeatures* function using the "vst" method. Clustering was performed using the
1095 Louvain method and a resolution of 1.15 in Seurat's *FindClusters* function.

1096 ***BCR sequence analysis and clonal clustering***

1097 BCR repertoire sequence data were analyzed using the Immcantation

1098 (www.immcantation.org) framework. Starting with filtered CellRanger output, V(D)J genes

1099 for each sequence were aligned to the IMGT GENE-DB reference database v3.1.29[69] using

1100 IgBlast v1.16.0[70] and Change-O v1.0.0[71]. Nonproductive sequences, cells without

1101 associated constant region calls, cells identified as arising from doublets or negative wells,

1102 and cells with multiple heavy chains were all removed. Samples within each subject were

1103 pooled and sequences were grouped into clonal clusters, which contain B cells that relate

1104 to each other by somatic hypermutations from a common V(D)J ancestor. Sequences were

1105 first grouped by common IGHV gene annotations, IGHJ gene annotations, and junction

1106 lengths. Using the hierarchicalClones function of *scoper* v1.1.0[72], sequences within these

1107 groups differing by a length normalized Hamming distance of 0.1 within the CDR3 region

1108 were defined as clones using single-linkage hierarchical clustering[73]. This threshold was

1109 determined through manual inspection of distance to nearest neighbor plots using *shazam*

1110 v1.1.0[74]. These heavy chain defined clonal clusters were further split if their constituent

1111 cells contained light chains that differed by V and J genes. Within each clone, germline

1112 sequences were reconstructed with D segment and N/P regions masked (replaced with

1113 "N" nucleotides) using the createGermlines function within *dowser* v0.1.0[75]. All BCR

1114 analyses used R v4.1.1 (R Core Team 2017), and plots were generated using *ggpubr*

1115 v0.4.0[76] and *ggplot2* v3.3.5[68]. After clonal clustering, only heavy chain sequences were

1116 used for subsequent analysis. Somatic hypermutation was calculated as the Hamming

1117 distance between each sequence's IMGT-gapped sequence alignment and its predicted

1118 unmutated germline ancestor along the V-gene (IMGT positions 1-312).

1119 Clonal diversity is an important metric of B cell repertoires, and low B cell clonal diversity

1120 is consistent with an adaptive immune response. To quantify B cell clonal diversity, we

1121 calculated Simpson's diversity for each sample using the alphaDiversity function of

1122 *alakazam* v1.1.0[71]. Lower values of Simpson's diversity indicate a greater probability of two

1123 random sequences belonging to the same clone, consistent with more large clones. To

1124 account for differences in sequence depth, samples within each comparison were down-

1125 sampled to the same number of sequences, and the mean of 1000 such re-sampling

1126　repetitions was reported. Only donor/tissue/cell sort samples with at least 100 B cells were

1127　included, which led to the exclusion of all S1^{+} cells from CNMC 99 (control with no history

1128　of COVID-19) and S1[+] PBMCs from CNMC 89 (COVID-19 convalescent). Clonal overlap

1129　among tissues can be used as a measure of immunological connectivity. Clonal overlap

1130　was calculated using the Jaccard index, which for each pair of tissues is the number of

1131　unique clones found in both tissues (intersect) divided by the total number of unique clones

1132　among the two tissues (union). Clones were labelled as "S1[+]" if they contained at least one

1133　S1[+] sorted B cell. To infer lineage trees, we estimated tree topologies, branch lengths, and

1134　subject-wide substitution model parameters using maximum likelihood under the GY94

1135　model[77,78]. Using fixed tree topologies estimated from the GY94 model, we then estimated

1136　branch lengths and donor-wide parameter values under the HLP19 model in IgPhyML

1137　v1.1.3[77]. Trees were visualized using *dowser* v0.1.0[75] and *ggtree* v3.0.4[79].

Whole slide multiplexed imaging of FFPE tissue sections

Tissue and slide processing and staining

1140　5 µm tissue sections were cut from FFPE samples and placed onto glass slides. Following

1141　sectioning, glass slides (with tissue) were baked in a 60°C oven for 1 hour.

1142　Deparaffinization was performed as described previously[80]: 2 exchanges of 100% xylene

1143　(10 minutes per exchange) followed by 100% ethanol for 10 minutes, 95% ethanol for 10

1144　minutes, 70% ethanol for 5 minutes, and 10% formalin for 15 minutes. Antigen retrieval

1145　was performed by incubating slides in AR6 buffer (Akoya Biosciences) for 40 minutes in a

1146　95°C water bath. After 40 minutes, slides were removed from the water bath and allowed

1147　to cool on the bench for 20 minutes. Sections were permeabilized, blocked, and stained in

1148　PBS containing 0.3% Triton X-100 (Sigma-Aldrich), 1% bovine serum albumin (Sigma-

1149　Aldrich), and 1% human Fc block (BD Biosciences). Immunolabeling was performed with

1150　the PELCO BioWave Pro 36500-230 microwave equipped with a PELCO SteadyTemp Pro

1151　50062 Thermoelectric Recirculating Chiller (Ted Pella) using a 2-1-2-1-2-1-2-1-2

1152　program[80,81]. A complete list of antibodies and imaging panels with labelling steps can be

1153　found in Supplementary Table 8. In general, primary antibodies were applied first, washed

1154　3 times in PBS, and incubated with appropriate secondary antibodies. Directly conjugated

1155　primary antibodies were applied last after blocking with host sera (5%). Endogenous biotin

1156 was blocked using the Avidin/Biotin Blocking Kit (Abcam). Cell nuclei were visualized with
1157 Hoechst (Biotium) and sections were mounted using Fluoromount G (Southern Biotech).

1158 ***Confocal microscopy, image analysis, and histo-cytometry***

1159 Images were acquired using an inverted Leica TCS SP8 X confocal microscope equipped
1160 with a 40X objective (NA 1.3), 4 HyD and 1 PMT detectors, a white light laser that produces
1161 a continuous spectral output between 470 and 670 nm as well as 405, 685, and 730 nm
1162 lasers. All images were captured at an 8-bit depth, with a line average of 3, and 1024x1024
1163 format with the following pixel dimensions: x (0.284 µm), y (0.284 µm), and z (1 µm).
1164 Images from whole tissue sections were tiled and merged using the LAS X Navigator
1165 software (LAS X 3.5.5.19976). Fluorophore emission was collected on separate detectors
1166 with sequential laser excitation of compatible fluorophores (3-4 per sequential) used to
1167 minimize spectral spillover. The Channel Dye Separation module within the LAS X
1168 3.5.5.19976 (Leica) was then used to correct for any residual spillover. Threshold
1169 identification, voxel gating, surface creation, and masking were performed as previously
1170 described using Imaris software (Imaris version 9.8.0, Bitplane AG)[82,83]. For publication
1171 quality images, gaussian filters, brightness/contrast adjustments, and channel masks were
1172 applied uniformly to all images.

1173 A combination of automatic and manual surface/contour creation methods were used to
1174 define germinal center (GC) regions of interest (ROI) with Imaris software (Imaris version
1175 9.8.0, Bitplane AG). GCs were identified as aggregations of 5 or more Ki-67^{+} nuclei. For
1176 each sample, whole tissue ROIs were generated using the Hoechst channel and surface
1177 function of Imaris. The resulting metric, total area of tissue imaged, was then used to
1178 normalize the number and size of GCs between samples.

1179 The number and phenotype of T cells inside and outside of the B cell follicle/GC were
1180 quantified using histo-cytometry[83]. Cells were segmented on Hoechst[+] nuclei and used to
1181 create surfaces. Channel statistics for all surfaces were exported into Excel (Microsoft) and
1182 converted to a csv file for direct visualization in FlowJo v10.6.1 (Treestar). Mean voxel
1183 intensities for all channels were plotted on a linear scale and used for gating distinct
1184 lymphocyte populations. B cell follicle and GC gates were defined using positional data on

1185   the HLA-DR$^+$CD3$^-$ and Ki-67$^+$ surfaces, respectively. These positional gates were applied

1186   to T cell surfaces to calculate the frequency of T cell phenotypes inside or outside of the

1187   follicle/GC as demonstrated previously[84,85]. T cell numbers were normalized across all

1188   samples to account for differences in the number of T cells analyzed per sample. Imaging

1189   data were exported and processed in Excel (Microsoft Office) and GraphPad Prism 8.2.1.

1190   **Activated induced marker (AIM) assay**

1191   Banked frozen PBMC and tonsil and adenoid cells were thawed as described above in

1192   "Processing for CITE-seq." Two million mononuclear cells from tonsil or adenoid or one

1193   million PBMC from each donor were cultured in a 96 well round bottom plate at a

1194   concentration of 1×10^7 cells/mL in media consisting of RPMI plus 5% human AB serum

1195   (Omega), 2 mM L-glutamine, 0.055 mM beta-mercaptoethanol, 1% penicillin/streptomycin,

1196   1 mM sodium pyruvate, 10 mM HEPES, and 1% non-essential amino acids. Cells were

1197   blocked at 37°C for 15 min prior to peptide pool stimulation with 0.5µg/mL of anti-CD40

1198   mAb (Miltenyi). Following this, cells were stimulated with SARS-CoV-2 peptide pools for

1199   18 hours at 37°C in 5% CO_2 incubator. The following peptide pools were reconstituted per

1200   instructions and used for stimulation (Miltenyi): PepTivator SARS-CoV-2 Prot_S+,

1201   PepTivator SARS-CoV-2 Prot_S1, PepTivator SARS-CoV-2 Prot_S, PepTivator SARS-

1202   CoV-2 Prot_N, PepTivator SARS-CoV-2 Prot_M. Prot_S+, Prot_S1 and Prot_S were

1203   pooled into one megapool of spike peptides at concentration of 0.6 nmol/ml for each pool.

1204   PHA-L (Millipore) at 5µg/ml was used as positive control. Negative control wells lacking

1205   peptides were supplemented with an equivalent volume of DMSO and ddH$_2$O. After

1206   stimulation, cells were first stained with a viability dye (LIVE/DEAD Blue, ThermoFisher)

1207   for 15 min at RT, washed twice and then incubated with True-Stain Monocyte Blocker

1208   (BioLegend) for 5 min. Antibodies for chemokine receptors (anti-CXCR3 for 10 min, anti-

1209   CCR7 for 10 min, anti-CXCR5 and anti-CCR6 together for 5 min) were sequential added

1210   at RT. The antibody cocktail containing the rest of the surface antibodies and Brilliant Stain

1211   Buffer Plus (BD) was then added directly to the cells and incubated for 30 min at RT in the

1212   dark (total staining volume 180uL). Stained cells were washed three times and fixed in 1%

1213   paraformaldehyde for 20 min at RT before collecting on the Aurora spectral cytometer

1214   (Cytek). Antibodies and reagents used in this assay are listed in Supplementary Table 8.

T cell functional assays - intracellular cytokine staining

Frozen cells were thawed as described in "Processing for CITE-seq." 2 million PBMC, adenoid, or tonsil cells from each sample were resuspended in 200 μL of complete RPMI medium containing 10% FBS (VWR), 2 mM glutamine, 0.055 mM beta-mercaptoethanol, 1% penicillin/streptomycin, 1 mM sodium pyruvate, 10 mM HEPES, and 1% non-essential amino acids. Cells were stimulated with PMA (50ng/ml, Sigma) and ionomycin (1000ng/ml, Sigma) for 2.5 h in the presence of anti-CD107a (BioLegend), GolgiSTOP (monensin, BD), and GolgiPlug (BFA, BD). After stimulation, surface markers were stained as described above in the AIM assay. Surface-stained cells were washed and fixed with Cytofix Fixation Buffer (BD) at RT for 20 min and washed with permeabilization buffer (eBioscience) twice. Then, the intracellular cytokine antibody mix was added for 30 min at RT (staining volume 50uL). Stained cells were collected on the Aurora spectral cytometer (Cytek). Antibodies used in this assay are listed in Supplementary Table 8.

Viral quantification in FFPE blocks by ddPCR

RNA was extracted from scrolls cut from FFPE tonsil and adenoid tissues using the RNeasy FFPE Kit (Qiagen) according to the manufacturer's protocol. A NanoDrop ND-1000 Spectrophotometer (Thermo Fisher Scientific) was used to quantify RNA concentrations. The QX200 AutoDG Droplet Digital PCR System (Bio-Rad) was used to detect and quantify SARS-CoV-2 RNA using the SARS-CoV-2 Droplet Digital PCR Kit (Bio-Rad), which contains a triplex assay of primers/probes aligned to the CDC markers for SARS-CoV-2 N1 and N2 genes and human *RPP30* gene. Ninety-six-well plates were prepared with technical replicates of up to 550 ng of RNA per well using the aforementioned kit according to the manufacturer's instructions. The QX200 Automated Droplet Generator (Bio-Rad) provided microdroplet generation, and plates were sealed with the PX1 PCR Plate Sealer (Bio-Rad) before proceeding with RT–PCR on the C1000 Touch Thermal Cycler (Bio-Rad) according to the manufacturer's instructions. Plates were read on the QX200 Droplet Reader (Bio-Rad) and analyzed using the freely available QuantaSoft Analysis Pro Software (Bio-Rad) to quantify copies of N1, N2 and RP genes per well, which was then normalized to RNA concentration input. For samples to be considered positive

1244 for SARS-CoV-2 N1 or N2 genes, they needed to average the manufacturer's limit of

1245 detection of ≥ 0.1 copies per µl and two positive droplets per well.

Statistics and reproducibility

1247 Please see above for a detailed description of statistical analysis of results from

1248 unsupervised analysis as well as where to find reproducible scripts. Simplified Presentation

1249 of Incredibly Complex Evaluation (SPICE) software (version 6, NIAID, NIH, Bethesda, MD,

1250 USA, https://niaid.github.io/spice/) was used to analyze flow cytometry data on T cell

1251 polyfunctionality[30]. Graphs were produced by Prism (v8). Statistical analyses were

1252 performed using SPSS (IBM, version 28.0.0.0). Differences between groups were

1253 compared using the Mann-Whitney U test for independent values and Wilcoxon signed

1254 ranks test for paired values. Correlations were assessed using the Spearman rank

1255 correlation. All statistical tests were two-sided. $p < 0.05$ was considered significant.

Methods References:

58 Michael, S. *et al.* Standardization of ELISA protocols for serosurveys of the SARS-CoV-2 pandemic using clinical and at-home blood sampling. *Nature communications* **12**, doi:10.1038/s41467-020-20383-x (2021).

59 Zahra, F. T., Bellusci, L., Grubbs, G., Golding, H. & Khurana, S. Neutralisation of circulating SARS-CoV-2 delta and omicron variants by convalescent plasma and SARS-CoV-2 hyperimmune intravenous human immunoglobulins for treatment of COVID-19. *Annals of the Rheumatic Diseases*, annrheumdis-2022-222115, doi:10.1136/annrheumdis-2022-222115 (2022).

60 Ravichandran, S. *et al.* Antibody signature induced by SARS-CoV-2 spike protein immunogens in rabbits. *Sci Transl Med* **12**, doi:10.1126/scitranslmed.abc3539 (2020).

61 Tang, J. *et al.* Antibody affinity maturation and plasma IgA associate with clinical outcome in hospitalized COVID-19 patients. *Nat Commun* **12**, 1221, doi:10.1038/s41467-021-21463-2 (2021).

62 Park, L. M., Lannigan, J. & Jaimes, M. C. OMIP-069: Forty-Color Full Spectrum Flow Cytometry Panel for Deep Immunophenotyping of Major Cell Subsets in Human Peripheral Blood. *Cytometry A* **97**, 1044-1051, doi:10.1002/cyto.a.24213 (2020).

63 Liu, C. *et al.* Time-resolved systems immunology reveals a late juncture linked to fatal COVID-19. *Cell* **184**, 1836-1857.e1822, doi:10.1016/j.cell.2021.02.018 (2021).

64 Kotliarov, Y. *et al.* Broad immune activation underlies shared set point signatures for vaccine responsiveness in healthy individuals and disease activity in patients with lupus. *Nat Med* **26**, 618-629, doi:10.1038/s41591-020-0769-8 (2020).

1281   65   Hao, Y. *et al.* Integrated analysis of multimodal single-cell data. *Cell* **184**, 3573-
1282   3587.e3529, doi:10.1016/j.cell.2021.04.048 (2021).
1283   66   Mulè, M. P., Martins, A. J. & Tsang, J. S. Normalizing and denoising protein
1284   expression data from droplet-based single cell profiling. *bioRxiv*,
1285   2020.2002.2024.963603, doi:10.1101/2020.02.24.963603 (2021).
1286   67   Gu, Z., Eils, R. & Schlesner, M. Complex heatmaps reveal patterns and
1287   correlations in multidimensional genomic data. *Bioinformatics* **32**, 2847-2849,
1288   doi:10.1093/bioinformatics/btw313 (2016).
1289   68   Wickham, H. *ggplot2: Elegant Graphics for Data Analysis*. 1 edn, (Springer, New
1290   York, NY, 2009).
1291   69   Giudicelli, V., Chaume, D. & Lefranc, M. P. IMGT/GENE-DB: a comprehensive
1292   database for human and mouse immunoglobulin and T cell receptor genes.
1293   *Nucleic Acids Res* **33**, D256-261, doi:10.1093/nar/gki010 (2005).
1294   70   Ye, J., Ma, N., Madden, T. L. & Ostell, J. M. IgBLAST: an immunoglobulin variable
1295   domain sequence analysis tool. *Nucleic Acids Res* **41**, W34-40,
1296   doi:10.1093/nar/gkt382 (2013).
1297   71   Gupta, N. T. *et al.* Change-O: a toolkit for analyzing large-scale B cell
1298   immunoglobulin repertoire sequencing data. *Bioinformatics* **31**, 3356-3358,
1299   doi:10.1093/bioinformatics/btv359 (2015).
1300   72   Nouri, N. & Kleinstein, S. H. A spectral clustering-based method for identifying
1301   clones from high-throughput B cell repertoire sequencing data. *Bioinformatics* **34**,
1302   i341-i349, doi:10.1093/bioinformatics/bty235 (2018).
1303   73   Gupta, N. T. *et al.* Hierarchical Clustering Can Identify B Cell Clones with High
1304   Confidence in Ig Repertoire Sequencing Data. *J Immunol* **198**, 2489-2499,
1305   doi:10.4049/jimmunol.1601850 (2017).
1306   74   Yaari, G. *et al.* Models of somatic hypermutation targeting and substitution based
1307   on synonymous mutations from high-throughput immunoglobulin sequencing data.
1308   *Front Immunol* **4**, 358, doi:10.3389/fimmu.2013.00358 (2013).
1309   75   Hoehn, K. B., Pybus, O. G. & Kleinstein, S. H. Phylogenetic analysis of migration,
1310   differentiation, and class switching in B cells. *bioRxiv*, 2020.2005.2030.124446,
1311   doi:10.1101/2020.05.30.124446 (2020).
1312   76   Kassambara, A. ggpubr: 'ggplot2' Based Publication Ready Plots version
1313   0.4.0.from GitHub. (2020).
1314   77   Hoehn, K. B. *et al.* Repertoire-wide phylogenetic models of B cell molecular
1315   evolution reveal evolutionary signatures of aging and vaccination. *Proceedings of*
1316   *the National Academy of Sciences* **116**, 22664-22672,
1317   doi:doi:10.1073/pnas.1906020116 (2019).
1318   78   Nielsen, R. & Yang, Z. Likelihood models for detecting positively selected amino
1319   acid sites and applications to the HIV-1 envelope gene. *Genetics* **148**, 929-936,
1320   doi:10.1093/genetics/148.3.929 (1998).
1321   79   Yu, G., Smith, D. K., Zhu, H., Guan, Y. & Lam, T. T.-Y. ggtree: an r package for
1322   visualization and annotation of phylogenetic trees with their covariates and other
1323   associated data. *Methods in Ecology and Evolution* **8**, 28-36,
1324   doi:doi:10.1111/2041-210X.12628 (2017).

1325 80 Radtke, A. J. *et al.* IBEX: an iterative immunolabeling and chemical bleaching
1326   method for high-content imaging of diverse tissues. *Nature Protocols* **17**, 378-401,
1327   doi:10.1038/s41596-021-00644-9 (2022).
1328 81 Radtke, A. J. *et al.* IBEX: A versatile multiplex optical imaging approach for deep
1329   phenotyping and spatial analysis of cells in complex tissues. *Proceedings of the*
1330   *National Academy of Sciences* **117**, 33455-33465,
1331   doi:doi:10.1073/pnas.2018488117 (2020).
1332 82 Radtke, A. J. *et al.* Lymph-node resident CD8α+ dendritic cells capture antigens
1333   from migratory malaria sporozoites and induce CD8+ T cell responses. *PLoS*
1334   *Pathog* **11**, e1004637, doi:10.1371/journal.ppat.1004637 (2015).
1335 83 Gerner, M. Y., Kastenmuller, W., Ifrim, I., Kabat, J. & Germain, R. N. Histo-
1336   cytometry: a method for highly multiplex quantitative tissue imaging analysis
1337   applied to dendritic cell subset microanatomy in lymph nodes. *Immunity* **37**, 364-
1338   376, doi:10.1016/j.immuni.2012.07.011 (2012).
1339 84 Sayin, I. *et al.* Spatial distribution and function of T follicular regulatory cells in
1340   human lymph nodes. *J Exp Med* **215**, 1531-1542, doi:10.1084/jem.20171940
1341   (2018).
1342 85 Preite, S. *et al.* Hyperactivated PI3Kδ promotes self and commensal reactivity at
1343   the expense of optimal humoral immunity. *Nat Immunol* **19**, 986-1000,
1344   doi:10.1038/s41590-018-0182-3 (2018).
1345

1346 **Data Availability**: As sequencing data were collected from children, who are considered

1347 a vulnerable population, raw CITE-seq data are available upon request to corresponding

1348 authors. All other data are provided with the article or upon request from the

1349 corresponding authors. Source data for figures will be provided with this article.

1350

1351 **Code Availability**: The R scripts used in this paper are available on

1352 https://github.com/kalpanamanthiram/Covid-Tonsil.

1353

1368

1369 **Author contributions**: K.M., P.M., P.L.S, and Q.X. conceived and designed the study.

1370 Q.X., K.M., A.J.R., J.C., J.T., G.G., S.S., S.R., J.K., M. Karkanitsa., J.S., H.K., M. Kirby,

1371 F.C., G.K., P.D., and G.S. performed experiments. Q.X, K.M., P.M-A., A.J.M, A.J.R., C.L.,

1372 J.K., K.B.H., S.S., S.R., F.C., A.S., and I.T.M. analyzed and interpreted results. K.M., P.M.,

1373 H.B., N.R., D.P., and L.G. developed patient recruitment materials and/or recruited

1374 participants. Q.X., P.M-A., A.J.M., A.J.R., K.B.H., L.K., S. Preite, R.A., S. Pittaluga, R.N.G.,

1375 S.M., D.S.C., A.S., S.K., S.H.K., K.S., J.S.T., P.M., P.L.S., and K.M. provided critical

1376 scientific input and/or reagents. K.M., P.L.S., and Q.X. wrote the initial draft of the paper.

1377 All authors contributed to the final review and editing of the paper.

1378

1379 **Competing interests**: S. Preite and A.S. are currently employees of AstraZeneca and may

1380 own stock or stock options. S.H.K. receives consulting fees from Peraton. K.B.H. receives

1381 consulting fees from Prellis Biologics.

1382

1383

1384

Extended Data Figure 1
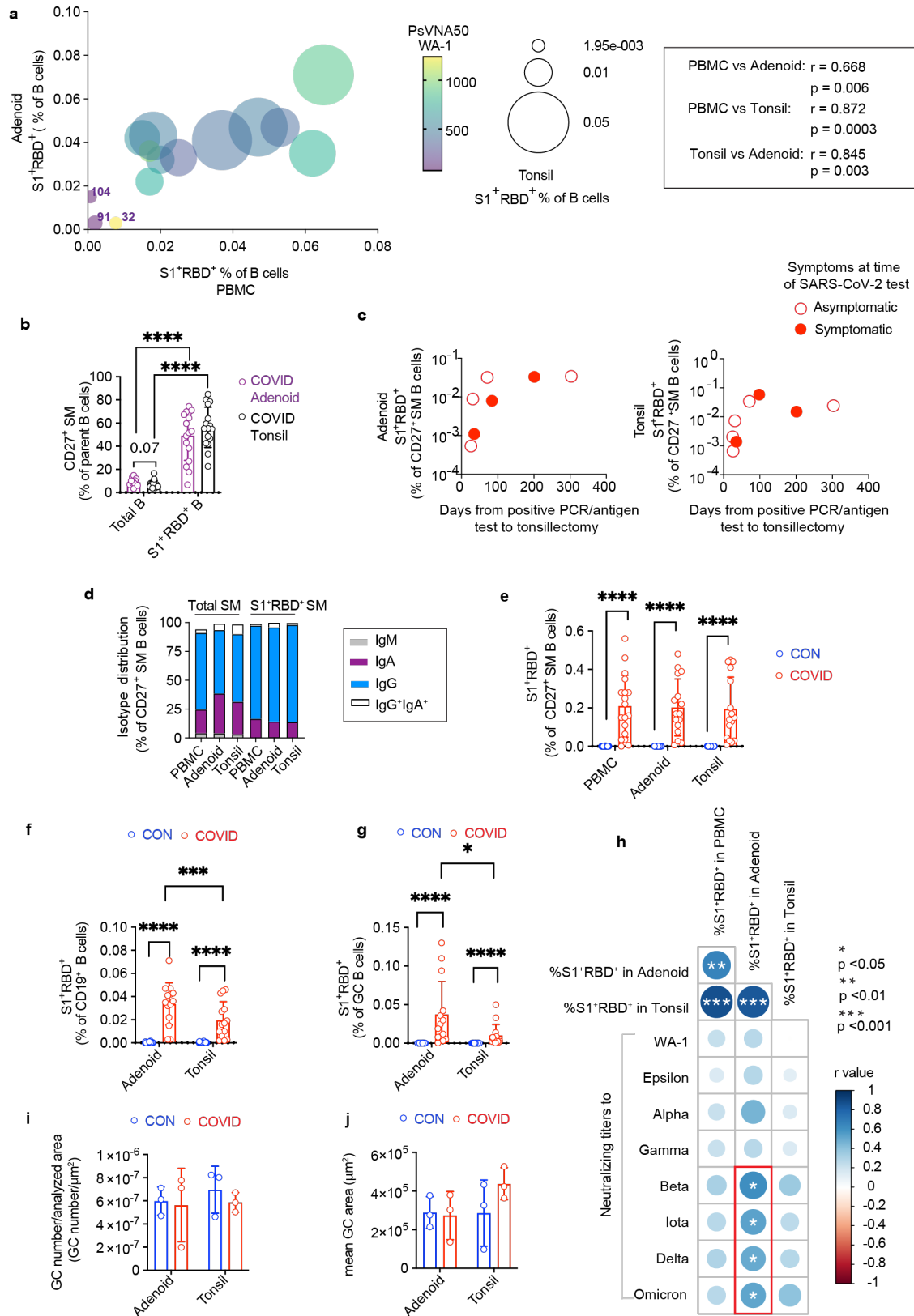
Extended Figure Data 1. Characterization of neutralization titers and S1⁺RBD⁺ B cells

a. Correlation among frequencies of S1$^+$RBD$^+$ cell among B cells in peripheral blood, tonsils, and adenoids. The color of data points indicates neutralizing titers (PsVNA50) to the WA-1 variant. Donors 32, 91, 104, who had the lowest frequencies of S1$^+$RBD$^+$ B cells, are labeled in the plot.

b. Frequency of CD27$^+$ switched memory (SM) B cells among total B cells and among S1$^+$RBD$^+$ B cells from adenoid and tonsil samples from COVID-19-convalescent participants

c. Frequency of S1$^+$RBD$^+$ cells among CD27$^+$ SM B cells in adenoid and tonsil according to time from presumed active infection (positive PCR/antigen test from nasopharyngeal swab) to surgery

d. Proportion of each isotype among S1$^+$RBD$^+$ SM B cells and total SM B cells in PBMC, adenoid, and tonsil following COVID-19. The percentage of IgA$^+$ cells was significantly lower among S1$^+$RBD$^+$ SM B cells compared to total SM B cells in the tissue ($p < 0.0001$ for adenoid, $p < 0.0001$ for tonsil).

e. Percentage of S1$^+$RBD$^+$ cells among CD27$^+$ SM B cells from PBMC, adenoid, and tonsil following COVID-19 (COVID) vs. controls (CON)

f and g. Percentage of S1$^+$RBD$^+$ cells among total B cells (f) and GC B cells (g) from 14 pairs of adenoid and tonsil COVID samples vs. CON

h. Summary of correlations among neutralizing titers (PsVNA50) against several SARS-CoV-2 variants and frequencies of S1$^+$RBD$^+$ cells among B cells in peripheral blood, adenoids, and tonsils.

i. and j. Mean number of GCs per total scanned tissue area (i) and mean GC area (total GC area in section/total number of GCs in section) (j) from adenoid and tonsil in COVID vs. CON samples. Samples imaged are in Supplementary Table 9.

Gating strategy is shown in Supplementary Fig. 1-2. Samples used in panels a-h are listed in Supplementary Table 2 and 4 (PBMC COVID n = 18, CON n = 33; adenoid COVID n = 16, CON n = 27; and tonsil COVID n = 16, CON n = 30). Each symbol represents data from one donor. Means ± S.D. are displayed in the scatter and bar plots. Significance calculated with Mann-Whitney U test for unpaired values or Wilcoxon signed ranks test for paired values from the same donor. Correlation analysis performed with Spearman's rank correlation. * $p<0.05$, *** $p<0.001$, **** $p<0.0001$.
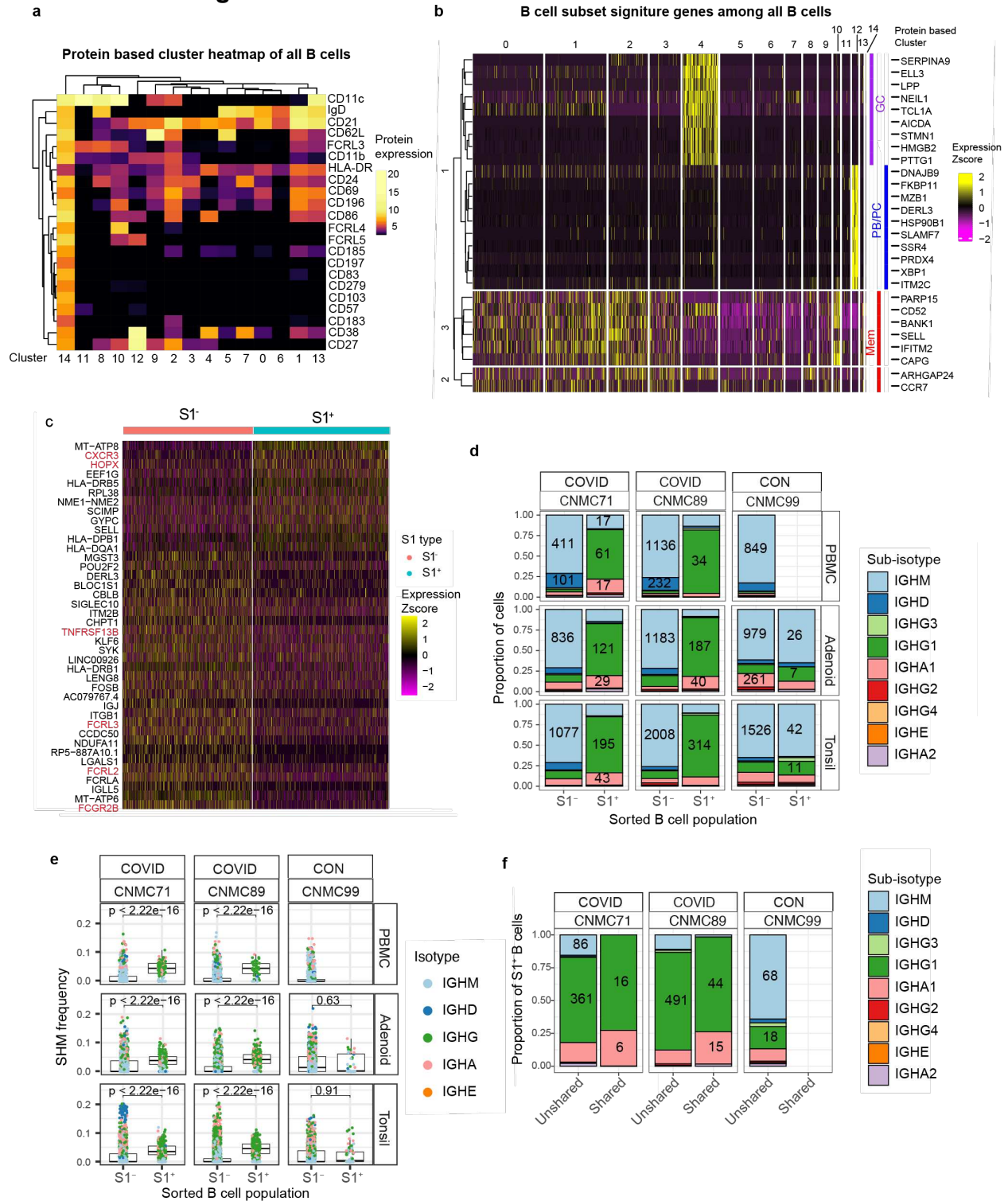
Extended Data Figure 2

1421 **Extended Data Figure 2. CITE-seq analysis of SARS-CoV-2 antigen-specific B cells**

1422 a. Heatmap of unsupervised clustering by CITE-seq antibody expression of S1⁺ and S1⁻ B

1423 cells from tonsil, adenoid, and PBMCs from three donors (2 COVID-19 convalescent and

60

1424   1 control) yielding 15 clusters. Most S1$^+$ B cells are in cluster 2 which is IgD$^-$ and CD27$^+$,

1425   indicative of a memory B cell phenotype.

1426   b. Heatmap showing expression of signature gene sets for germinal center (GC) B cells,

1427   memory B cells, and plasma cells/plasmablasts (PC/PB) among all B cells (S1$^+$ and S1$^-$)

1428   from tonsil, adenoid, and PBMC

1429   organized by cluster.

1430   c. Heatmap showing differentially expressed (DE) genes in S1$^+$ vs. S1$^-$ B cells from tonsil

1431   and adenoid from cluster 2 (which are CD27$^+$ memory B cells, shown in Fig. 2a and

1432   Extended Data Fig. 2a). DE gene list is in Supplementary Table 5.

1433   d. Sub-isotype frequencies among S1$^+$ and S1$^-$ B cells from adenoid, tonsil and PBMC of

1434   two COVID-19 convalescent donors (CNMC 71 and 89) and one control (CNMC 99).

1435   Labels show the raw number of cells with a given sub-isotype and are only shown for sub-

1436   isotypes that make up at least 10% of a given category.

1437   e. Somatic hypermutation (SHM) frequency among S1$^+$ and S1$^-$ B cells of all isotypes from

1438   PBMC, adenoid, and tonsil of each donor. Mutation frequency calculated in V gene.

1439   Significance calculated with the Mann Whitney U test.

1440   f. Sub-isotype frequencies among S1$^+$ B cells from clones shared between tonsil and

1441   adenoid vs. unshared clones. Labels show the raw number of cells with a given sub-isotype

1442   and are only included for sub-isotypes that make up at least 10% of a given category.

1443

1444
1445

Extended Data Figure 3

1448 **Extended Data Figure 3. Gene-based clustering of CITE-seq of S1$^+$ and S1$^-$ B cells**

1449 Unsupervised clustering based on gene expression of sorted S1$^+$ and S1$^-$ B cells from

1450 tonsil, adenoid, and PBMCs from three donors (2 COVID-19 convalescent and 1 control)

1451 yielding 19 clusters. Top defining genes for each cluster are noted. Top bar shows the

1452 corresponding cluster based on CITE-seq surface protein expression (shown in Extended

1453 Data Fig. 2a-b); middle bar indicates which cells are S1$^+$, and lower bar indicates tissue of

1454 origin.

1455

1456 **Extended Data Figure 4**
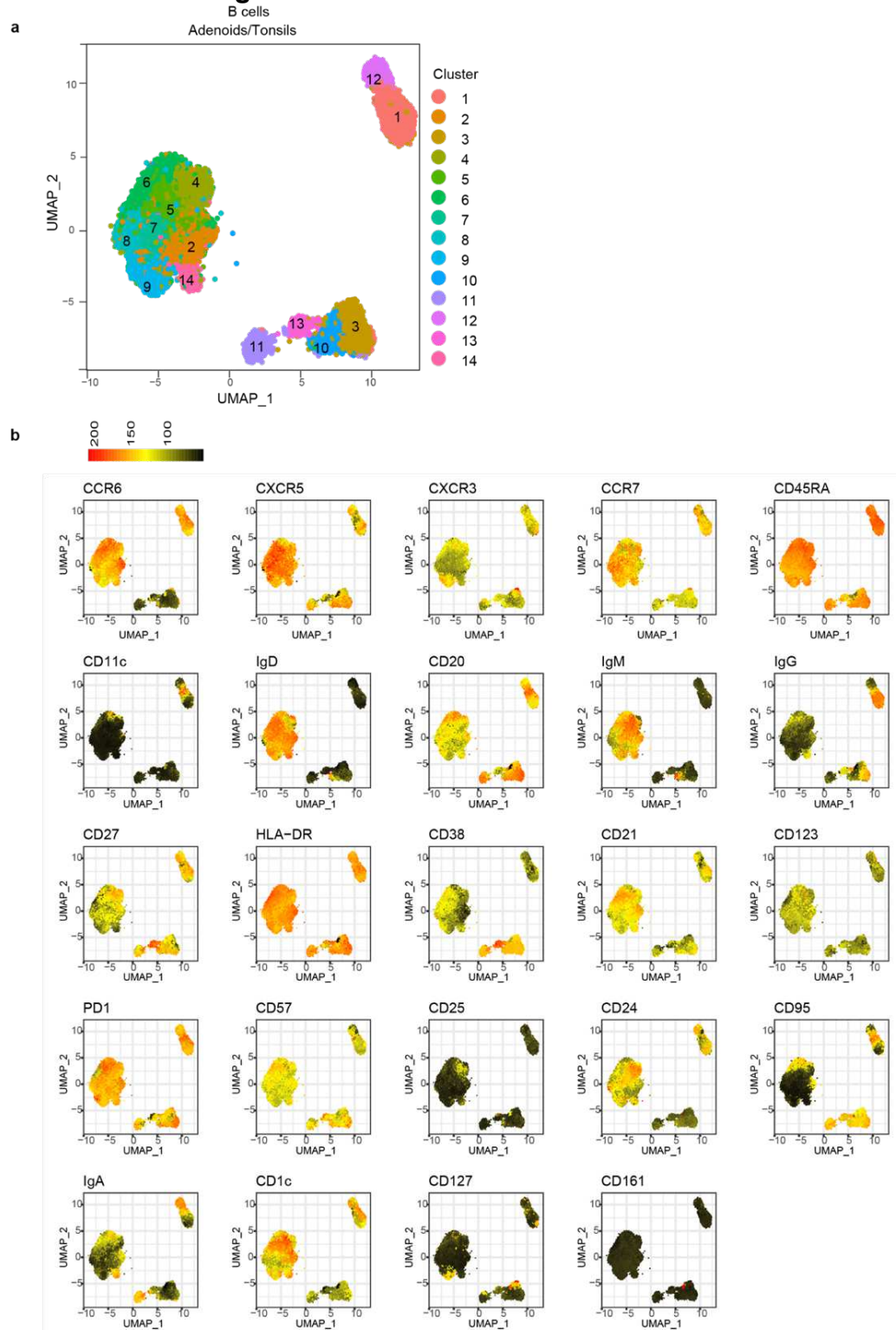
1457
1458 **Extended Data Figure 4. UMAP of unsupervised clustering of B cells from tonsil and**

1459 **adenoid**

1460 a. Uniform manifold approximation and projection (UMAP) of unsupervised clustering of

1461 surface markers from flow cytometric analysis of CD19$^+$ B cells from adenoid and tonsil.

1462 b. Heatmaps of marker/antibody expression overlayed on UMAP.

1463

Extended Data Figure 5
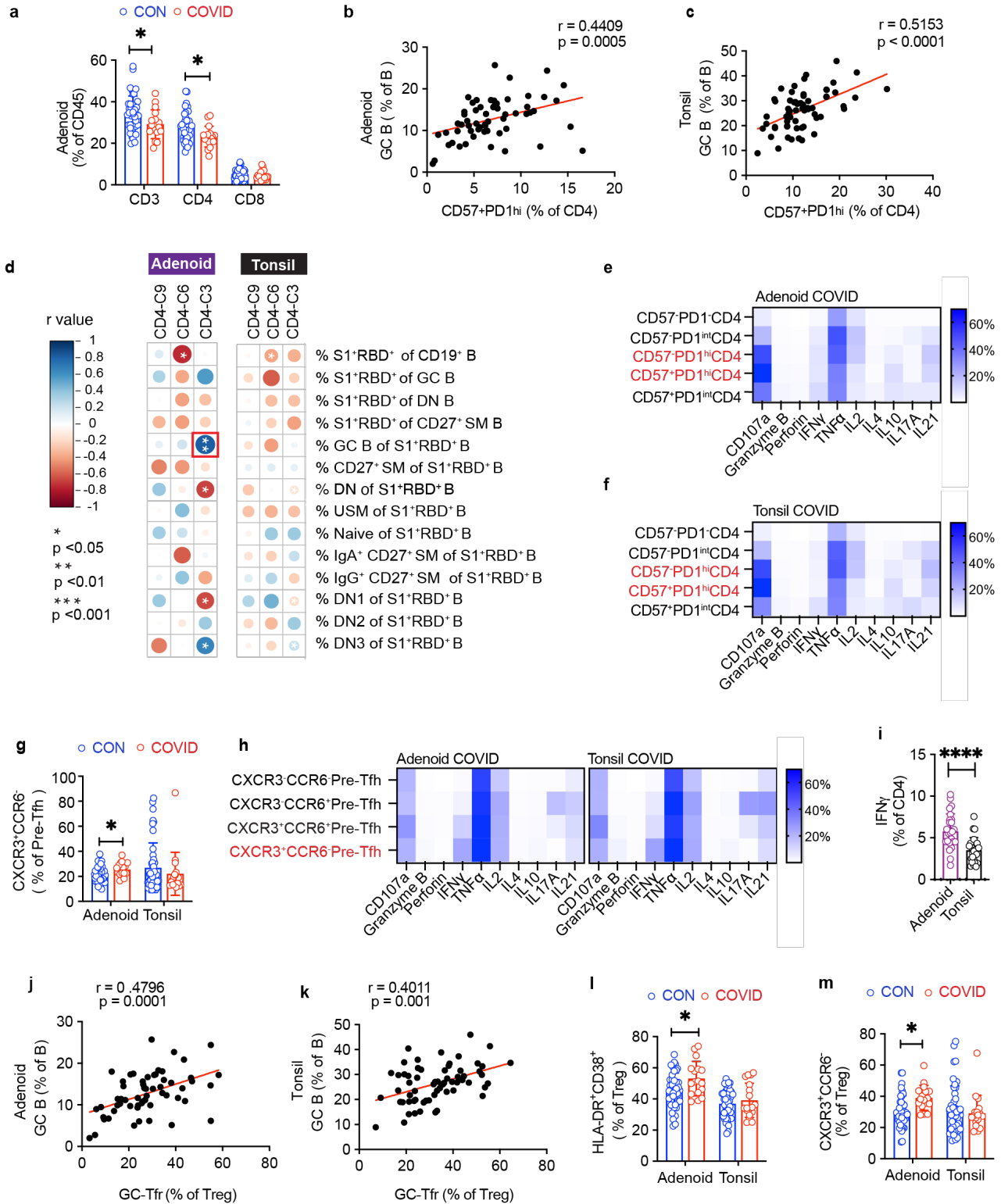
1467 **Extended Data Figure 5. Phenotyping of expanded CD4⁺ T cell populations in tissue**

1468 a. Comparison of CD3$^+$, CD4$^+$, and CD8$^+$ T cell frequency in adenoid of COVID-19-
1469 convalescent donors (COVID) vs. controls (CON).

1470 b and c. Correlation between frequency of CD57$^+$PD-1^{hi} CD4$^+$ T cells and frequency of GC
1471 B in adenoids (b) and tonsil (c) (adenoid n = 59, tonsil n = 64, includes both COVID-19-
1472 convalescent samples and controls).

1473 d. Summary of correlations among various subsets of SARS-CoV-2 antigen-specific B cells
1474 and significantly different clusters from unsupervised analysis of tissue CD4$^+$ T cells
1475 (clusters 3, 6, 9). USM = unswitched memory B, SM = switched memory B, DN = double
1476 negative B, GC = germinal center.

1477 e and f. Intracellular cytokine and cytotoxic factor expression in various CD4$^+$ T cell subsets
1478 gated on CD57 and PD-1 from COVID-19-convalescent adenoids (e, n = 13) and tonsil (f,
1479 n = 13) after PMA and ionomycin stimulation. Mean frequency expressing each cytokine is
1480 plotted in the heatmap.

1481 g. Frequency of CXCR3$^+$CCR6$^-$ cells among pre-Tfh cells (PD-1^{int}CXCR5$^+$ conventional
1482 CD4$^+$ T) in adenoids and tonsils of COVID vs. CON.

1483 h. Intracellular cytokine and cytotoxic factor expression in different pre-Tfh cell subsets
1484 gated on CXCR3 and CCR6 from COVID-19-convalescent adenoids (n = 13) and tonsils
1485 (n = 13) after PMA and ionomycin stimulation. Mean frequency expressing of each cytokine
1486 is plotted in the heatmap.

1487 i. Comparison of IFN-γ production by CD4$^+$ T cells in adenoid versus tonsil following
1488 PMA/ionomycin stimulation (n = 26 which includes 13 COVID and 13 CON of each tissue).

1489 j. Correlation between frequency of GC-Tfr and GC B frequencies in adenoid (n = 59,
1490 includes both COVID and CON).

1491 k. Correlation between frequency of GC-Tfr and GC B frequencies in tonsil (n = 64, includes
1492 both COVID and CON).

1493 l and m. Frequencies of HLA-DR$^+$CD38$^+$ (d) CXCR3$^+$CCR6$^-$ (e) cells among Treg cells in
1494 adenoid and tonsil. (COVID adenoid n = 17, CON adenoid n = 42, COVID tonsil n = 18,
1495 CON tonsil n = 46).

1496 Gating strategy shown in Supplementary Fig. 5. Samples analyzed in panels a-c, g and j-
1497 m are listed in Supplementary Table 2 (COVID adenoid n = 17, CON adenoid n = 42,
1498 COVID tonsil n = 18, CON tonsil n = 46). Samples analyzed for panel d-e and h-i are in

1499   Supplementary Table 9. Each symbol represents data from one donor. Means ± S.D. are

1500   displayed on scatter and bar plots. Significance calculated using Mann-Whitney U test to

1501   compare two groups and Spearman's rank test for correlations.   * p<0.05

1502

1503 **Extended Data Figure 6**
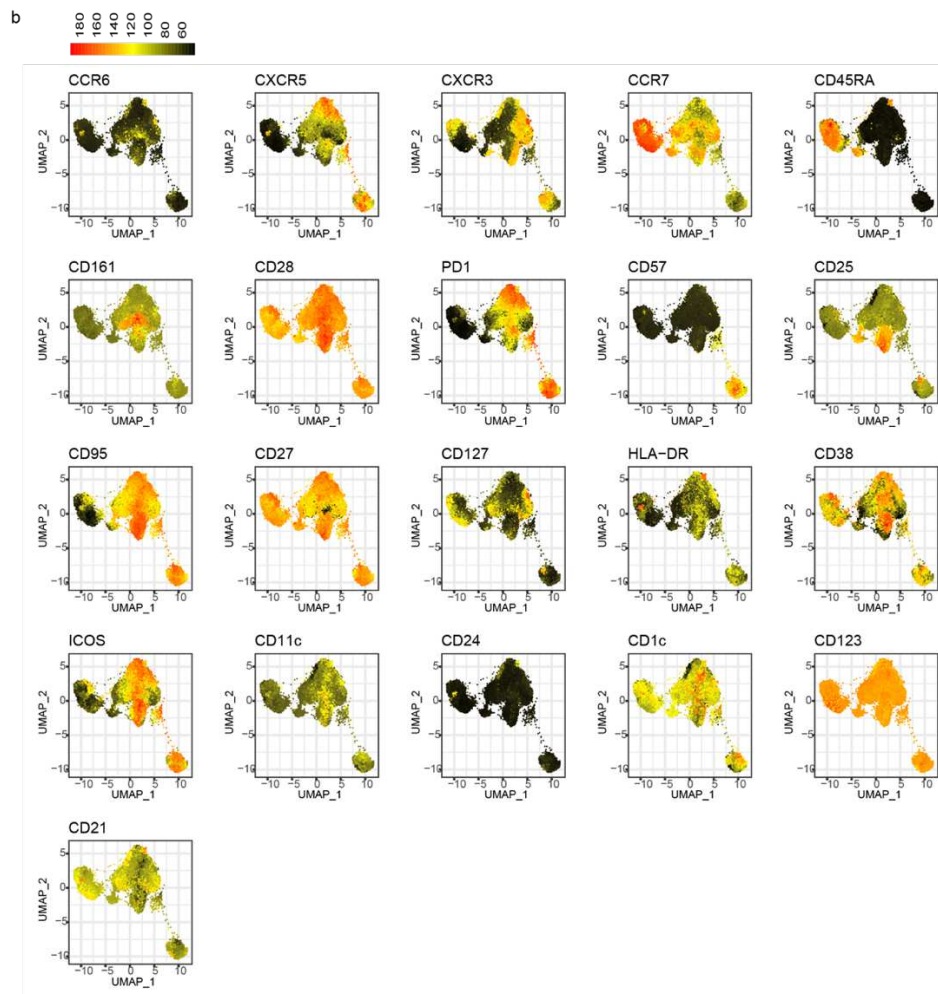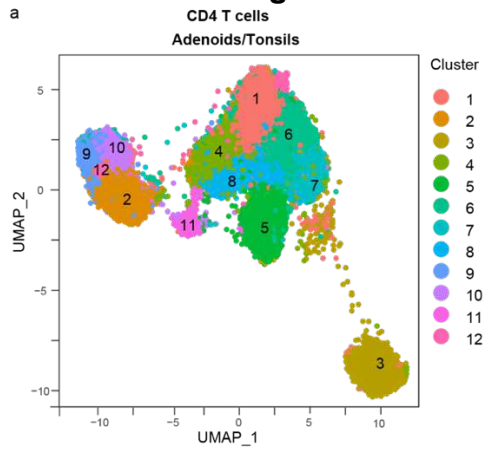
1504

1505 **Extended Data Figure 6. UMAP of unsupervised clustering of CD4$^+$ T cells from tonsil**

1506 **and adenoid**

1507   a. Uniform manifold approximation and projection (UMAP) of unsupervised clustering of

1508   surface markers from flow cytometric analysis of CD4$^+$ T cells from adenoid and tonsil.

1509   b. Heatmaps of marker/antibody expression overlayed on UMAP.

1510

1511 **Extended Data Figure 7**
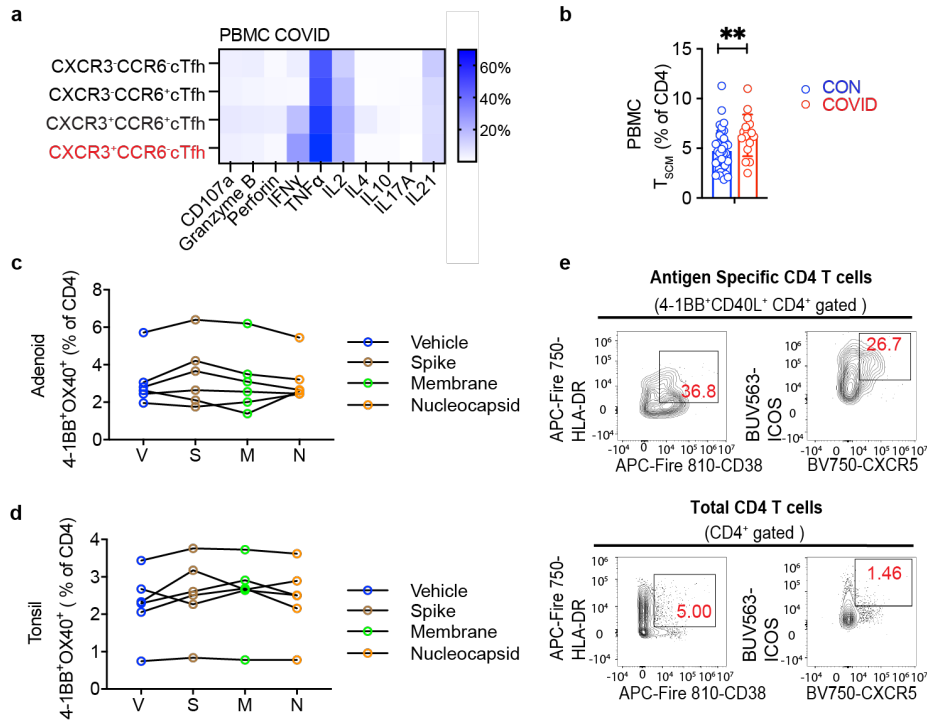
1512

1513

1514 **Extended Data Figure 7. SARS-CoV-2 antigen-specific CD4$^+$ T cells following COVID-**

1515 **19**

1516 a. Intracellular cytokine and cytotoxic factor production by various circulating Tfh (cTfh)

1517 cell subsets in PBMC gated by CXCR3 and CCR6 from COVID-19-convalescent donors

1518 (n = 4) following PMA and ionomycin stimulation. Mean frequency expressing each

1519 cytokine is plotted in heatmap.

1520 b. Frequency of stem cell-like memory CD4$^+$ T (T$_{SCM}$,

1521 CD45RA$^+$CCR7$^+$CD28$^+$CD27$^+$CD95$^+$) subsets in PBMC of COVID-19-convalescent

1522 donors (COVID) vs. controls (CON) (COVID = 16, CON = 41). Significance calculated

1523 using Mann-Whitney U test. Gating strategy in Supplementary Fig. 7.

1524 c and d. Frequencies of AIM$^+$ (OX40$^+$4-1BB$^+$) CD4$^+$ T cells from adenoid (c) and tonsil (d)

1525 of COVID-19-convalescent donors following SARS-CoV-2 peptide pool stimulation

1526 (adenoid n = 6, tonsil n = 6). Significance calculated with Wilcoxon signed rank test for

1527 paired samples from the same donor.

1528 e. Flow cytometry plots showing frequency of HLA-DR$^+$CD38$^+$ and ICOS$^+$CXCR5$^+$ cells

1529 from concatenated antigen-specific CD4$^+$ T cells from PBMC following SARS-CoV-2

1530 peptide stimulation compared to total CD4$^+$ T cells. AIM$^+$ CD4$^+$ T cells were concatenated

1531 from all three peptide pool stimulations of PBMCs from all 6 donors.

1532 Samples analyzed in panel a, c, and d are listed in Supplementary Table 9, and in panel b

1533 are in Supplementary Table 2. ** p<0.01.

1534

1535 **Extended Data Figure 8**
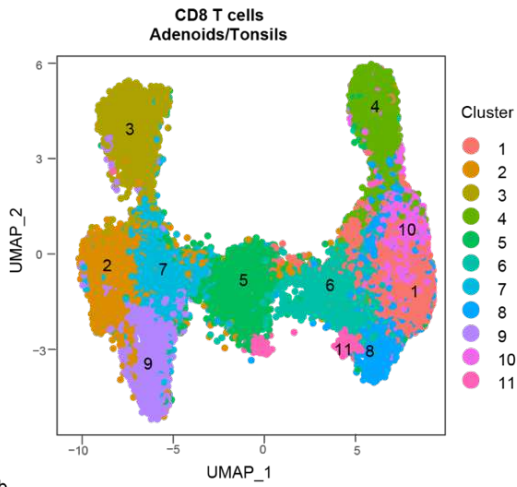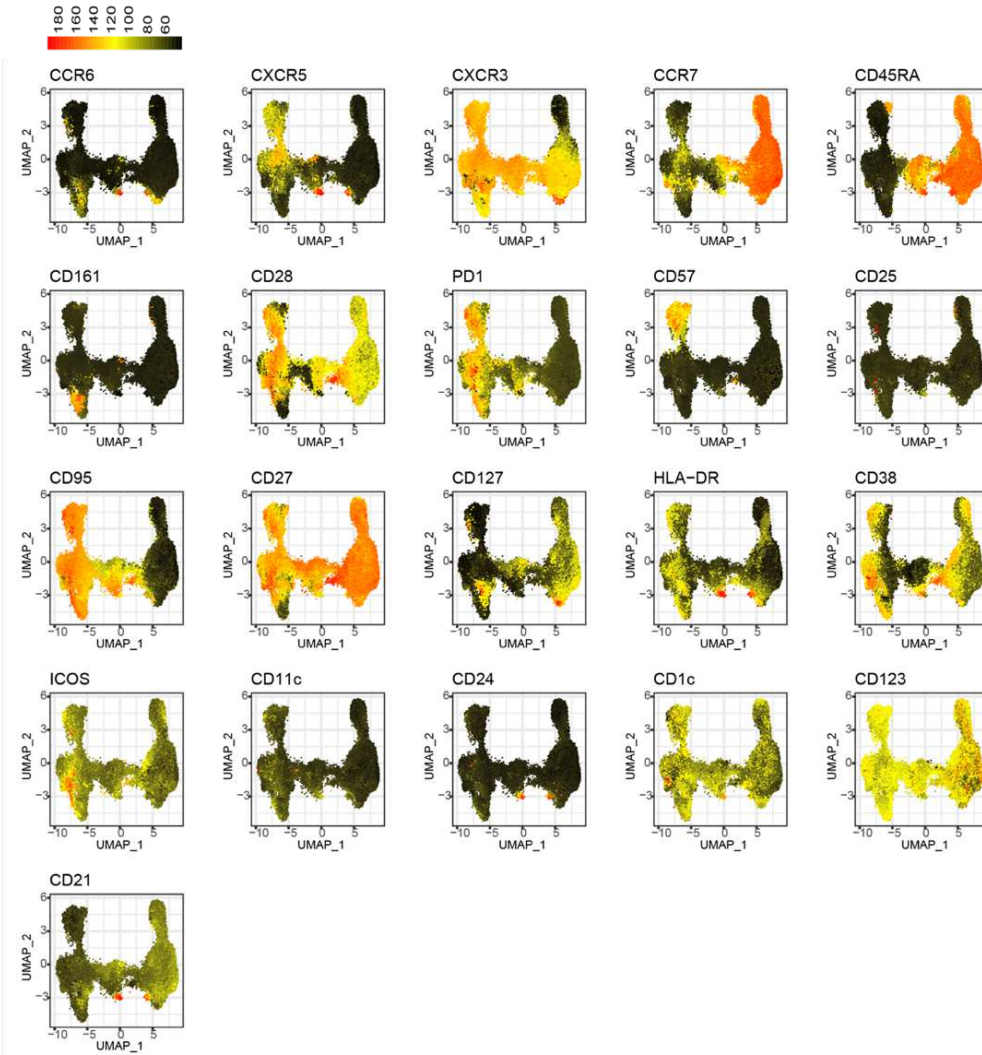
1536

1537 **Extended Data Figure 8. UMAP of unsupervised clustering of CD8⁺ T cells from tonsil**

1538 **and adenoid**

1539   a. Uniform manifold approximation and projection (UMAP) of unsupervised clustering of

1540   surface markers from flow cytometric analysis of CD8$^+$ T cells from adenoid and tonsil.

1541   b. Heatmaps of marker/antibody expression overlayed on UMAP.
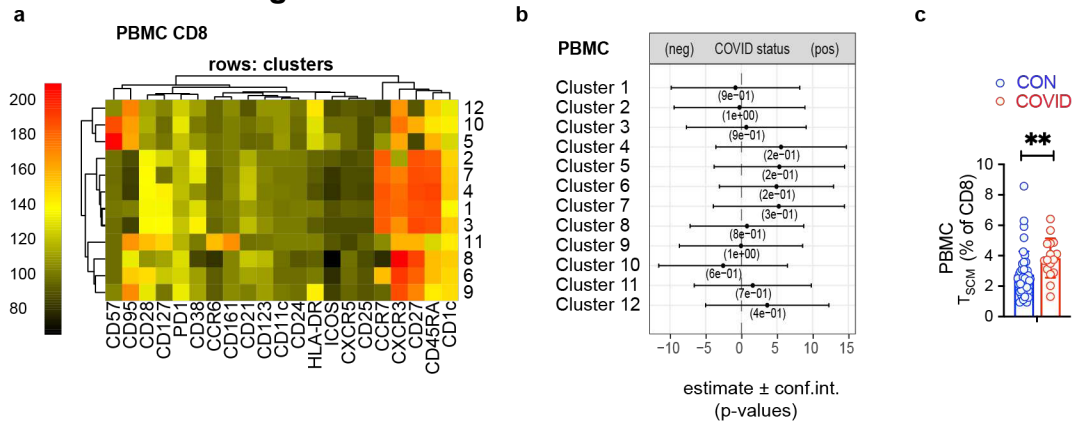
1542

Extended Data Figure 9
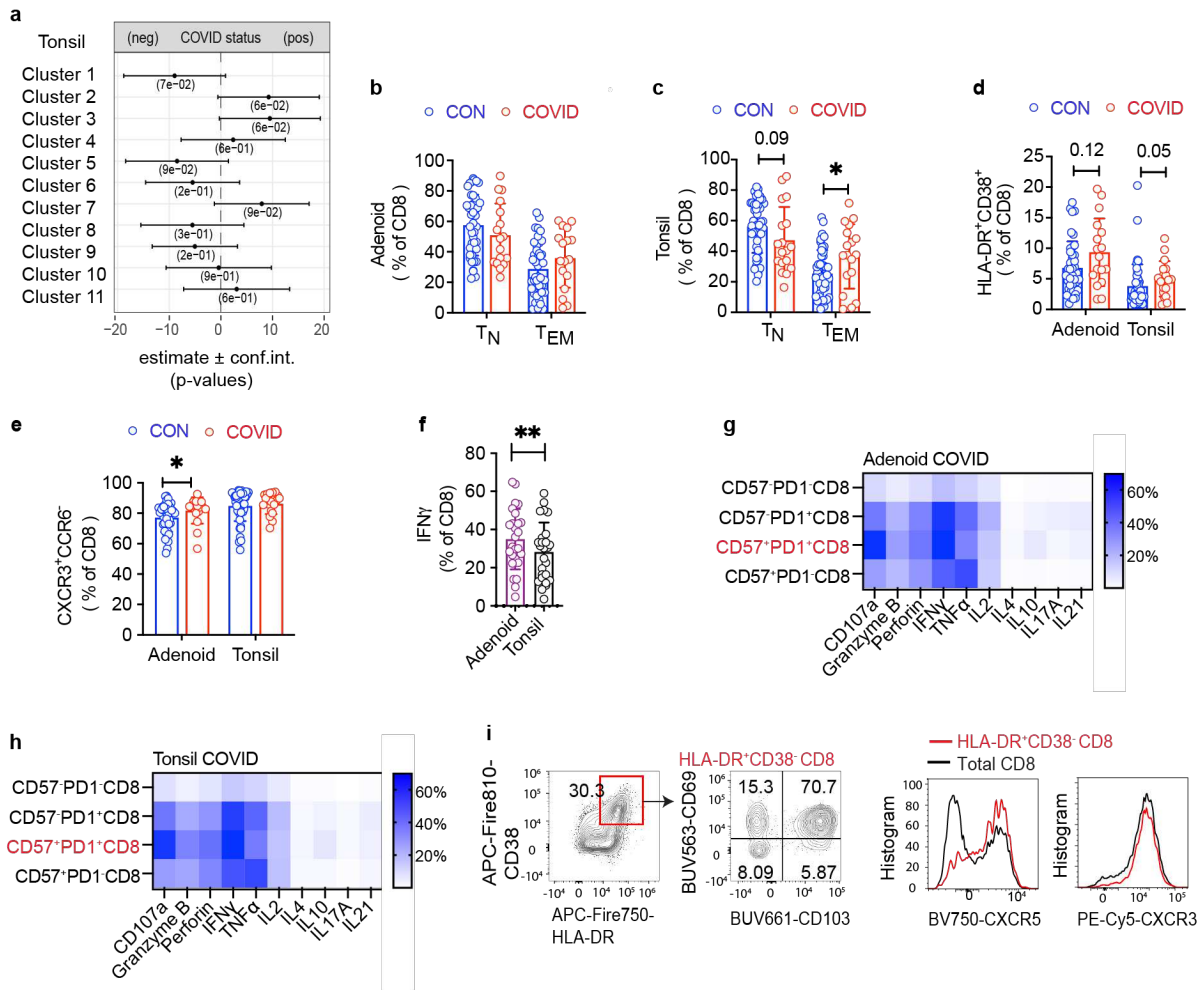
1547 **Extended Data Figure 9. Phenotyping of CD8$^+$ T cells from tonsil and adenoid**

1548

1549 a. Quantification of the effect of prior SARS-CoV-2 infection on CD8$^+$ T cell clusters in tonsil

1550 estimated with a linear model controlling for age and sex. Regression coefficients with 95%

1551 confidence intervals and p values are shown (COVID n = 15, CON n = 42).

1552 b and c. Frequencies of naïve (T$_N$, CD45RA$^+$CCR7$^+$) and effector memory (T$_{EM}$, CD45RA$^-$

1553 CCR7$^-$) CD8$^+$ T cells in adenoid (b) and tonsil (c) of COVID-19-convalescent samples

1554 (COVID) vs. controls (CON).

1555 d and e. Frequency of HLA-DR$^+$CD38$^+$ (d) and CXCR3$^+$CCR6$^-$ (e) cells among CD8$^+$ T cells

1556 in adenoid and tonsil from COVID vs. CON.

1557 f. Comparison of IFN-γ production by CD8$^+$ T cells in adenoid versus tonsil following PMA

1558 and ionomycin stimulation (n = 26 which includes 13 COVID and 13 CON of each tissue).

g and h. Intracellular cytokine and cytotoxic factor production by different CD8$^+$ T cell subsets gated by CD57 and PD-1 from adenoid (g, n = 13) and tonsil (h, n = 13) from COVID-19-convalescent donors. Mean expression of each cytokine is plotted in the heatmap.

i. Representative flow cytometry plots showing the expression of CD69, CD103, CXCR3, and CXCR5 levels on HLA-DR$^+$CD38$^+$ CD8$^+$ T cells in tonsil. Phenotypes are similar in adenoid.

Gating strategy shown in Supplementary Fig. 5. Samples analyzed in panels a-e are listed in Supplementary Table 2 (COVID adenoid n = 17, CON adenoid n = 42, COVID tonsil n = 18, CON tonsil n = 46), and in panel f-h are in Supplementary Table 9. Each symbol represents data from one donor. Means ± S.D. are displayed on scatter and bar plots. Significance calculated using Mann-Whitney U test. * p<0.05, ** p<0.01.

Extended Data Figure 10

Extended Data Figure 10. Phenotyping of CD8⁺ T cells from PBMC

a. Unsupervised clustering of CD8$^+$ T cells from PBMC according to surface antibodies from flow cytometric analysis. No clusters showed significant differences ($p<0.05$) in COVID-19-convalescent samples (COVID) vs. controls (CON) (COVID n = 13, CON n = 34).

b. Quantification of the effect of prior SARS-CoV-2 infection on CD8$^+$ T cell clusters in PBMC estimated with a linear model controlling for age and sex. Regression coefficients with 95% confidence intervals and p values are shown. So significantly different clusters were found. Statistical analysis is described in Methods.

c. Frequency of T stem cell-like memory (T_{SCM}, CD45RA$^+$CCR7$^+$CD28$^+$CD27$^+$CD95$^+$) among CD8$^+$ T cells in PBMC of COVID (n = 16) vs CON (n = 41). Gating strategy shown in Supplementary Fig. 8. Means ± S.D. are displayed on scatter and bar plots. Significance calculated using Mann-Whitney U test.

Samples analyzed are listed in Supplementary Table 2. Each symbol represents data from one donor. ** $p<0.01$

Supplementary Files

This is a list of supplementary files associated with this preprint. Click to download.

- SupplementaryTable4SerologicTestSummaryandData.xlsx
- SupplementaryFigures20220318.pdf
- SupplementaryTable5DEGenesS1PositivevsS1NegativeBcells.xlsx
- SupplementaryTable3CharacteristicsofParticipantswithCOVID19.docx
- SupplementaryTable10UnsupervisedAnalysisofFlowCytometryData.xlsx
- SupplementaryTable1DemographicCharacteristicsofParticipants.docx
- SupplementaryTable2ParticipantCharacteristicsandSummaryofSamplesUsedinImmuneProfiling.xlsx
- SupplementaryTable7ddPCRResultsfromFFPE.xlsx
- SupplementaryTable2ParticipantCharacteristicsandSummaryofSamplesUsedinImmuneProfiling.xlsx
- SupplementaryTable6CharacteristicsofSharedClones.xlsx
- SupplementaryTable3CharacteristicsofParticipantswithCOVID19.docx
- SupplementaryTable8Reagents.xlsx
- SupplementaryTable4SerologicTestSummaryandData.xlsx
- SupplementaryTable5DEGenesS1PositivevsS1NegativeBcells.xlsx
- SupplementaryTable10UnsupervisedAnalysisofFlowCytometryData.xlsx
- SupplementaryTable6CharacteristicsofSharedClones.xlsx
- SupplementaryTable9SamplesusedinFunctionalAnalysesandImaging.xlsx
- SupplementaryTable7ddPCRResultsfromFFPE.xlsx
- SupplementaryTable1DemographicCharacteristicsofParticipants.docx
- SupplementaryFigures20220318.pdf
- SupplementaryTable8Reagents.xlsx
- SupplementaryTable9SamplesusedinFunctionalAnalysesandImaging.xlsx